공학박사 학위논문

Optimized Photoexcitation of TiO_2 Nanostructures for Energy and Environmental Applications

이산화티탄 나노구조체의 에너지 및 환경분야 응용을 위한 광여기 최적화

2019년 2월

서울대학교 대학원

화학생물공학부

이 수 영

Abstract

Optimized Photoexcitation of TiO_2 Nanostructures for Energy and Environmental Applications

Su Young Lee
School of Chemical and Biological Engineering
The Graduate School
Seoul National University

Titanium dioxide (TiO_2)-based nanostructures have attracted attention as an excellent material for solar energy conversion with photocatalysts and photovoltaics (solar cells) and solving environmental problems through the decomposition of organic pollutants in environmentally friendly ways. Economic feasibility, outstanding physical and chemical stability, and ease of band-gap control make TiO_2 more attractive than other semiconducting materials for photoconversion. Applying TiO_2

nanostructures to the energy and environment fields utilizing solar energy is a very important technology because it can provide solutions beyond the limit of fossil fuels and environmental problems as a mean of clean and renewable energy. It is therefore important to exploit the advantages of TiO_2, meanwhile, the band gap is wide (3.0 to 3.2 eV) to effectively utilize visible light, which is a significant portion in solar energy spectrum, and also there is a limit that the photon-to-energy conversion efficiency becomes low because of the recombination of photoexcited charge carriers. In this study, approaches to optimized photoexcitation of TiO_2 nanostructures on the different aspects are provided to solve the above problems. The contents including the approach in the structural aspect to improve the light harvesting efficiency, and in the material aspect to control the electronic structure and interface are presented.

TiO2 nanotube arrays heterojunctioned with silver nanoparticles (Ag NPs) were fabricated to control the efficiency of photoexcitation not manipulating the intrinsic properties of TiO_2, which is an indirect optimization of the system. Regularly arranged TiO_2 nanotube arrays have the characteristics of photonic crystal and exhibit structural absorptions rather than absorption by the band-gap of the material.

Based on the results of finite difference time-domain (FDTD) simulation, structural parameters of TiO_2 nanotube arrays were designed and optimized to match the structural absorption band to the plasmonic absorption band from Ag NPs. TiO_2 nanotube arrays with matched absorption bands showed a photocurrent density three times improved under the visible light irradiation over 400 nm or more as compared with TiO_2 nanotube arrays with mismatched absorption bands. The study suggests that the rational design is important to optimize the photoexcitation in plasmonic photon-to-energy conversion systems based on metal oxides with a wide band gap including TiO_2.

To directly optimize the performance of photoexcited nano TiO_2 catalysts by controlling the electronic structure and the interface, TiO_2 nanoparticles were prepared by combining with metal cocatalysts and applied to the gas-phase acetaldehyde decomposition as a model reaction. Fundamental surface characterization techniques were used to explain the enhanced photocatalytic performance. The synthetic conditions were optimized to ensure effective operation under visible light and economic feasibility. The optimized nanocatalyst maintained its photocatalytic performance only with 0.1 wt % of Pt, which is about a tenth of Pt content compared to the commercial catalysts.

Keywords: photoexcitation, titanium dioxide, solar energy conversion, TiO_2 nanostructures, surface plasmon effect, LSPR, metal cocatalysts, gas-phase acealdehyde decomposition

Student Number: 2013-22530

Contents

List of Tables

List of Figures

Chapter 1. Introduction

1.1 TiO_2 nanostructures for solar energy conversion

Fossil fuels, which are non-renewable and finite energy sources have drawn many economic and environmental problems for decades.[1, 2] In this point of view, renewable energy resources such as wind and solar energy have been considered as promising energy sources for the future generation due to their infiniteness and cleanness. They do not raise any concern about meeting the energy demand over the world. Especially, sunlight, or solar energy, is known to deliver 1.2×10^5 terawatts of energy to Earth continuously.[3] It far exceeds the rate of global energy consumption, currently about 18.3 terawatts in 2016.[4] Solar energy can be converted into electricity via photovoltaics, chemical fuels via natural and artificial photosynthesis, and heat.

Taking the importance of harvesting the solar energy into consideration, TiO_2 has emerged as one of the most attractive

materials these days. Outstanding properties of TiO_2 such as chemical stability, photostability, and semiconducting character made it possible to be applied for solar energy conversion.[5-8] TiO_2 nanostructures have been widely used in photocatalysis, air and water purification, and photoelectrochemical water splitting to utilize solar energy (**Figure 1-1**).[7, 9-14] In both electron harvesting and photocatalysis, size, surface area, crystalline phase, pore structure, and many other physical properties affect the performance. Since all these physical properties are important, it is necessary to design the structure for the purpose.[2, 7] In addition, the dimension of structure is also a factor affecting the electronic structure of TiO_2 and photocatalytic and photoelectrochemical performance. The bandgap widened by the quantum confinement effect in nanoscale structures gives TiO_2 the prolonged lifetime of photogenerated charges and the enhanced redox ability. Besides, zero-dimensional spherical nanoparticles have a high

specific surface area and are advantageous for aqueous phase photocatalytic reaction due to the short diffusion length required for the photogenerated charges. It is possible to decompose organic compounds in the solution rapidly.[15] Structures such as one-dimensional nanotubes and nanofibers can also reduce recombination rate due to the short diffusion lengths of photogenerated charges as in zero-dimensional nanoparticles.[16, 17] It should be focused that the regularly arranged nanotubes have the property of photonic crystal that makes it possible to control the light utilization efficiency through the structural absorption.[18] Two-dimensional nanosheets and three-dimensional nanoarchitecture also have the advantages of high carrier mobility.[19, 20] Although the stcurture in each dimension own its unique property, this study deals with photoexcitation of TiO_2 consisting of a one-dimensional nanotube and a zero-dimensional nanoparticle.

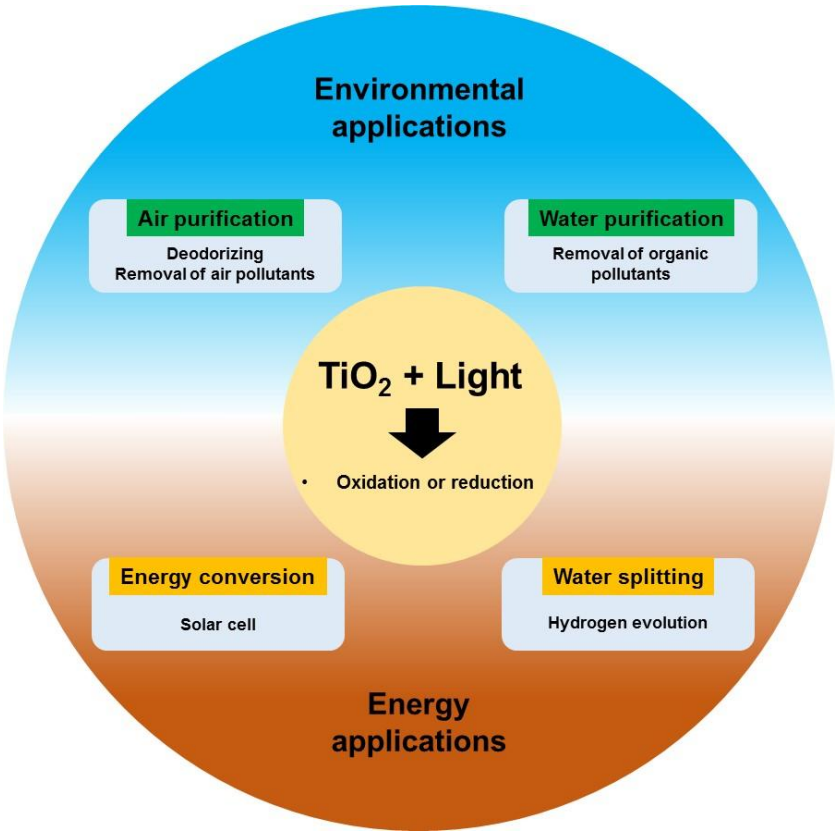

Figure 1-1. Energy and environmental applications of photoexcited TiO_2.[7]

1.2 Fundamentals of photoexcitation process in TiO_2

1.2.1 Primary steps of photoexcitation in TiO_2

To maximize efficiency of photoexcitation, it is important to understand the fundamental mechanism of TiO_2 and to use it to design materials and structures. TiO_2 commonly has a rutile or anatase phase. Rutile has a band gap of 3.0 eV and anatase has a bandgap of 3.2 eV, which are large not enough to absorb the visible light.[21] Even though TiO_2 is responsive to UV light, it can be prepared to work under the visible light by modifying the electronic structure through various methods such as hetero-element doping or heterojunction with other semiconductor materials.[10, 12, 22-27] The phenomenon occurring inside TiO_2 when light is irradiated is as follows.[7] When TiO_2 absorbs the light with the energy larger than the bandgap energy, electrons are excited from the valence band to the conduction band remaining holes in the valence band, which is called charge separation.

Separated electrons and holes migrate to the surface of TiO_2 and take parts in the redox reactions or are collected into the external circuit.[28] The trapping of the separated charges is completed within 300 femtoseconds, which is faster than the charge recombination (1~10 picoseconds for surface recombination). The recombination is inevitable, however, because the timescale of interfacial charge transfer reaches 300 picoseconds to 100 microseconds (**Figure 1-2**)[28, 29].

1.2.2 Photoexication in metal/TiO_2 composites

The photocatalytic performance can be enhanced by modifying TiO_2 with metal nanoparticles resulting in an improved charge separation.[30-35] Usually the noble metals are used to form metal/TiO_2 composites. The enhanced charge separation is attributed to the electric field formed at the interface of TiO_2 and metal by the

simultaneous migration of photogenerated electrons and holes to the bulk and the surface, respectively.[36] The energy barrier is shown in **Figure 1-3**. The energy barrier is called Schottky barrier, which is the driving force of this type of charge migration facilitating the charge separation spatially.[37] Noble metals serve as electron sinks due to the large work functions compared to n-type TiO_2 and also act as active sites.

Upon the illumination of metal/TiO_2, the influence of the excitation of the metal particle on the dynamics of the photogenerated charges needs to be considered. The metal nanoparticles can be characterized by their surface plasmon resonance (SPR), which is the photo-induced collective oscillations of electrons at the surface of metal nanoparticles.[28] An increased local electromagnetic field is generated upon the illumination of the metal/TiO_2.[38-40] The interaction of the localized electric field with TiO_2 induces the

formation of charge carriers near the surface. These mobile charge carriers easily reach the surface sites on TiO_2. This enhances the electron–hole separation and possibly leads to an increased photocatlytic performance under the visible light.

The electrons originated from the SPR effect, which are called hot electrons, has been promoting the concept of assembling metal nanoparticles with semiconductors including TiO_2.[41-45] Pt/TiO_2 composites can only be excited by UV light, while Ag/TiO_2 and Au/TiO_2 are excitable in the visible light region. This desirable plasmonic property of the noble metals are exploited in this study.

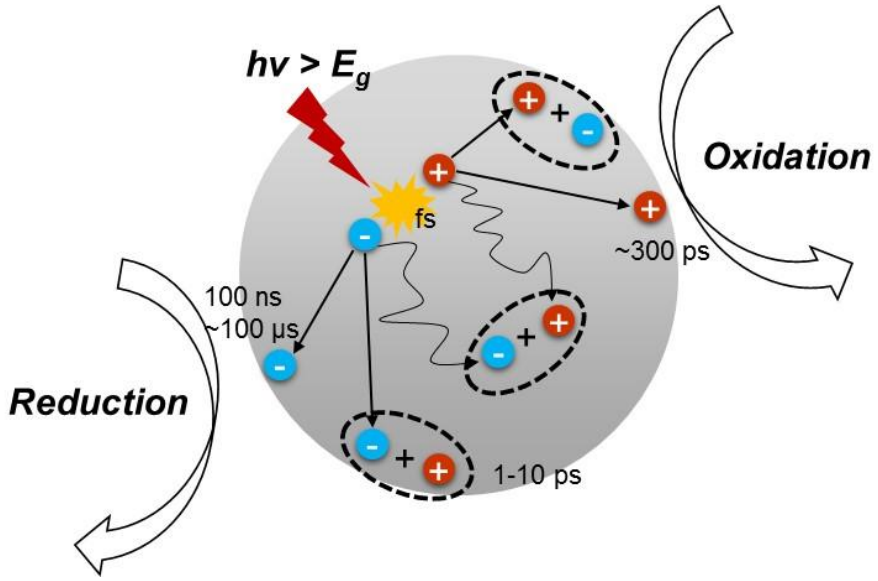

Figure 1-2. Primary fate of the photogenerated electrons and holes in TiO_2 nanomaterials. Dashed circle indicates the recombination.

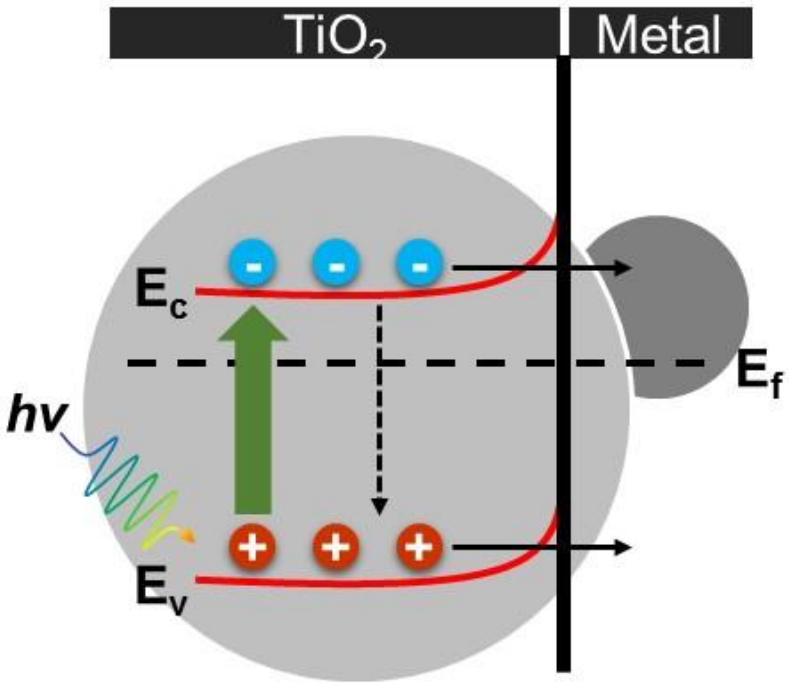

Figure 1-3. Photoexcitation process and band diagram of a common metal/TiO_2 composite under the light irradiation with larger energy than the bandgap of TiO_2.

1.3 Objectives

The objective of the thesis is to suggest the methods to design and optimize photoexcitation of TiO_2 nanostructures to effectively apply TiO_2 in energy and environmental fields. As seen in the Introduction part, the major limitations in using a wide bandgap TiO_2 are low photoconversion efficiency because of the poor absorption from solar spectrum and the fast recombination of charge carriers. Strategies can be provided in two different aspets.

In Chapter 2, the approach in the structural aspect to improve the light harvesting efficiency, an indirect approach in the way that it does not manipulate the intrinsic electronic properties of TiO_2, is suggested. TiO_2 nanotube arrays heterojunctioned with Ag NPs are discussed to investigate the synergetic effect between structural absorption and plasmonic absorption.

In Chapter 3, the direct approach in the material aspect to control the electronic structure and the interface of TiO_2 by combining with metal nanoparticles as cocatalysts was suggested. In particular, economic feasibility of Pt/TiO_2 which is available under the visible light was highlighted. Improved photocatalytic performance is discussed focusing on the gas-phase acetaldehyde decomposition as a model reaction.

Consequently, the strategies to improve the photoexcitation of TiO_2 nanostructures introduced in this thesis will be informative for understanding and desigining the rational TiO_2 nanocomposites for solar energy conversion.

Chapter 2. Development of a $SrTiO_3/TiO_2$ photonic heterostructure for the plasmon-induced electron harvesting

2.1 Introduction

Well-designed nanoheterostructure of semiconductor has drawn great interest for years due to its wide application in developing the photosystem such as photocatalytic organic degradation, photoelectrochemical water splitting, artificial photosynthesis and photovoltaics.[46-50] As the most used semiconductor material for light harvesting system, TiO_2 is favored thanks to its suitable band structure for various redox reactions, photostability, and low cost. Particularly, one-dimensional TiO_2 nanotube arrays (1D TNAs) have been in the spotlight as a photoelectrode for effective photon-to-

electron conversion.[51-53] 1D TNAs provide aligned channels for the directional charge transport and short diffusion length thus minimizing the loss of electrons at the grain boundaries. They also provide a large specific surface area, which is favourable for the heterostructure facilitating the charge separation. However, TNAs themselves showed relatively low photon-to-electron conversion efficiency because of the large bandgap of TiO_2 and still fast recombination of electron/hole pairs.

Surface plasmon resonance, the collective oscillation of conduction electrons, at metal surfaces has been an important tool in a wide spectrum of research area including bio-imaging and sensing.[54, 55] Especially the localized surface plasmon resonance (LSPR), which arises from the small metal nanostructures, has been used as a kind of strategies to enhance the efficiency of solar energy conversion.[56, 57] The LSPR bands are adjustable from UV to near-IR region by simply

modifying the properties of the surrounding environment such as materials, the structure, and the dielectric properties.[58, 59] It makes a strong absorption of the visible light at specific wavelengths possible with the plasmonic metals acting as photosensitizers, and results in the enhanced electron collection under the visible light. However, there still remains a lot of challenges to efficiently utilize these hot electrons because they are quickly relaxed through scattering with other electrons and phonons within the several to hundreds of femtoseconds timescale.[60] Prolonged lifetime of hot electrons or faster electron transfer are required to maximize the effect of plasmons.

The concept proved in intense studies has shown that the plasmon-induced hot electrons are injected into the adjacent semiconductors.[41] A Schottky barrier developed between metal and semiconductor facilitates the transfer of hot electrons to the conduction band (CB) of semiconductor. This novel interaction has been applied in previous

researches by junctioning the plasmonic metal nanoparticles and various semiconductor materials to achieve the improvement in harvesting of plasmon-induced hot electrons.[61] As one of the most favored semiconductor materials for the plasmonic heterostructure, 1D TNAs would fully take the advantages mentioned above to be an efficient photoelectrode.

In efforts to enhance the photon-to-electron conversion, TNAs were coupled with conductive materials or other semiconductors to induce the effective charge separation as well as being doped with cations/anions to utilize visible light.[62, 63] In one particular approach, $SrTiO_3$ nanoparticles grown on surface of TNAs enhanced the energetics for photocatalysis by shifting the Fermi level of the heterostructure more negative.[64] $SrTiO_3$ also acts as a good electron filter to facilitate the charge transfer, which resulted in increased photoelectrochemical performance. Therefore, the heterostructure

could be a good substrate for photon-to-electron conversion system.

Prepared $SrTiO_3/TiO_2$ heterostructures also share the characteristics of photonic crystal which traps and localizes the light of specific wavelengths in ordered structure. The structural absorption of photonic crystal is simply tuned by adjusting the parameters such as pore diameter and interpore distance. Therefore, $SrTiO_3/TiO_2$ could enhance the PEC performance by hybridizing with photonic materials which require the absorption at specific wavelengths such as plasmonic metal NPs.

In this research, we present a novel three-component light harvesting system ($Ag/SrTiO_3/TiO_2$) which combines two important factors: (1) improved charge transfer via heterojunction of $SrTiO_3$ and TiO_2 and (2) enhanced absorption at specific wavelength due to the matched absorption bands of $SrTiO_3/TiO_2$ and Ag. As is well known, Ag NPs show the better optical properties compared to other plasmonic metal

NPs such as Au and Cu. The three-component system is designed by tuning the absorption wavelength of $SrTiO_3/TiO_2$ to match the peak wavelength of Ag plasmon. In order to find the optimal structure of $SrTiO_3/TiO_2$ for the band alignment, absorption spectrum of Ag/ $SrTiO_3/TiO_2$ was simulated via finite-difference time domain (FDTD) method and consequently colud enhance the plasmon-induced charge separation.

2.2 Experimental

2.2.1 Fabrictaion of TNAs

TNAs were fabricated via a two-step anodization method. A Ti foil (99.7%, 0.127 mm thickness, Sigma-Aldrich) was cut into 1 cm × 4 cm pieces. Surface of the pieces was cleaned by sonicating in acetone, ethanol, followed by deionized water (DI water). A piece of cleaned Ti

sheet was used as an anode to be anodized with a Pt mesh as a cathode in a two-electrode system equipped with a DC power supply (PAP-3001, Powertron). The electrolyte in the system was composed of 97 vol % of ethylene glycol (99.9%, Samchun), 3 vol % of DI water, and 0.5 wt % NH_4F (≥98.0%, Sigma-Aldrich). The Ti sheet immersed in the electrolyte was first anodized at 60 V for 1 h. The TiO_2 layer which was formed during the anodization of Ti sheet was completely exfoliated by using a scotch tape and sonication in an ethanol/DI water mixed solution. The second anodization was performed under the same electrolyte at 60 V for 25 s to obtain TNAs which show the photonic absorption in the visible light around 430 nm. The temperature was maintained at 15 ^{o}C through an external temperature-control device during the anodization. The resulting TNAs were calcined under the air atmosphere at 450 ^{o}C for 4 h.

2.2.2 Formation of $SrTiO_3/TiO_2$ heterostructure

$SrTiO_3$ nanoparticles were grown on the surface of TNAs by a simple hydrothermal method. The TNAs fabricated above acted as a structural template on which $SrTiO_3$ nanoparticles were formed through the cation exchange. A piece of TNA sheet was first immersed in 0.025 M, 85 mL aqueous solution of $Sr(OH)_2 \cdot 8H_2O$. The solution was transferred to a Teflon cylinder, then the cylinder was sealed in a Teflon-lined stainless steel autoclave. The autoclave was heated at 180 ^oC for 1 h in the furnace. Ti^{4+} ions on the surface of TNAs were partially exchanged with Sr^{2+} ions forming $SrTiO_3$ nanoparticles during the hydrothermal reaction.[64]

2.2.3 Coupling Ag nanoparticles with $SrTiO_3/TiO_2$ heterostructure

Sheets of TNAs were first placed on a 4-inch Si wafer, which was used as a substrate for the thermal evaporation process. The Si wafer was put into a thermal chamber. Then Ag film was deposited uniformly on the wafer during the thermal evaporation process. Taken out from the chamber, $SrTiO_3/TiO_2$ on which Ag film was deposited (Ag-film/$SrTiO_3/TiO_2$) were detached from the wafer and washed with ethanol and DI water. The pieces of Ag-film/$SrTiO_3/TiO_2$ were annealed under 10% H_2/Ar mixed gas atmosphere at 300 ^oC in the purpose of dewetting the Ag film into nano-sized particles. Obtained Ag NPs/$SrTiO_3/TiO_2$ was characterized and analysed by photoelectrochemical measurements.

2.2.4 Characterization

The morphology and 2D elemental mapping of the Ag/$SrTiO_3/TiO_2$

were investigated by scanning transmission electron microscopy (STEM, JEM-2100F, 200 kV) equipped with the energy dispersive spectroscopy (EDS). Crystalline phase of each component was examined by X-ray diffraction (XRD, D/max-2500/PC, Rigaku) with Cu Kα radiation (λ = 0.154 nm) as the incident beam at 50 kV and 100 mA. Optical absorpbance were investigated by ultraviolet-visible diffuse reflectance spectroscopy (UV-DRS, V670-Jasco) with BaSO4 as a reference. Ag $3d^{5/2}$ spectra of $Ag/SrTiO_3/TiO_2$ with different dewetting times were obtained and used to calculate the surface content of Ag^0 by X-ray photoelectron spectroscopy (XPS, Thermo) where the binding energy was corrected with reference to the C 1s peak of 284.5 eV.

2.2.5 Computational details

OptiFDTD version 13.0 was used to perform the FDTD simulations.

The model was simulated by obtaining the air holes in TiO_2 arranged in a hexagonal lattice. The pore diameter was set to 100 nm and the inter-pore distance to 140 nm. The thickness of the film was ~200 nm. For a 3D simulation, mesh parameters were 0.006 μm × 0.006 μm × 0.009 μm, and time step size was set to 1.230e−017 with 1408 time steps. A rectangular input field with sine-modulated Gaussian pulse at 650 nm was used along the z-axis. Periodic boundary condition (PBC) was applied to x and y-direction, and anisotropic perfectly matched layer (APML) to z-direction.

2.3 Results and discussion

2.3.1 Material and structural characterization

The targeted heterostructure was composed of three components, which were Ag NPs, $SrTiO_3$ NPs, and TiO_2 nanotube arrays (TNAs). **Scheme 2-1** shows the fabrication steps of the heterostructure. TNAs were prepared by a simple two-step anodization method in the ehtyleneglycol as an electrolyte containing NH_4F, and small amount of water. $SrTiO_3$ NPs were deposited on the surface of calcinated TNAs by a hydrothermal method in the presence of Sr^{2+} source for a cation exchange. Parts of surface Ti^{4+} ions were exchanged with Sr^{2+} ions from $Sr(OH)_2$ thus forming crystalline $SrTiO_3$ NPs (**Figure 2-1**). Both TiO_2 and $SrTiO_3$ were so stable that can provide a heterostructure for better charge separation as intended. Ag NPs were deposited on $SrTiO_3/TiO_2$ by thermal evaporation process and the followed

annealing process under H_2/Ar atmosphere. **Figure 2-2** shows a STEM image and SEM images of the prepared Ag/$SrTiO_3$/TiO_2 heterostructure. TNAs showed a highly ordered porous structure being added on a Ti foil with diameter of the top open pores at about 100 nm and walls thickness in the range of 45~70 nm. The thickness of the bottom TNAs is 120 ~ 150 nm (**Figure 2-3**). Concaves shown in the top layer are expected to operate as nano-sized mirrors for the efficient light trapping. The structure of the TNAs in this study was determined by the anodization voltage and time which were controlled to maximize the structural absorption of TNAs in LSPR range of Ag NPs on the substrate. The results of 2D elemental mapping are also presented, which confirms that Ag and $SrTiO_3$ NPs were successfully formed on the surface of TNAs with high dispersity (**Figure 2-2**). Evenly dispersed $SrTiO_3$ NPs act as an excellent electron filter and the mid-state for energy cascade of electrons as planned in the designed

band structure of heterostructures (**Scheme 2-2**). As a result, $Ag/SrTiO_3/TiO_2$ was rationally designed in order to trap and localize the light in TNAs with photonic crystal property and thus the flux of light which were not directly absorbed could be reflected and scattered taking a chance for further utilization.

2.3.2 Computational and experimental design of optical properties

It has been reported that plasmon resonance is observed near spherical Ag NPs around 400 nm. Plasmonic Ag NPs can change their resonant frequency depending on the dielectric constant around them, and resonant frequencies tend to show red shifts when they are adjacent to the semiconducting materials. Based on the information, the ordered nanotube arrays with structural absorption band in the range of 400 ~ 500 nm were designed. In FDTD simulation, the model was simulated by obtaining the air holes in TiO_2 arranged in a hexagonal lattice.

When the pore diameter was set to 100 nm and the inter-pore distance to 140 nm, structural absorption of TNAs was obtained in a range of 400-500 nm, which is not the electronic bandgap of TiO_2 (**Figure 2-4**). The thickness of TNAs was less than 200 nm when TNAs were fabricated through an anodization method with the second anodization step for < 1 min. Thickness within this range did not affect the simulation results dramatically. The exact fabrication of TNAs was not easy to follow the computational design because of irregularity and slight peak shift occurred during the calcination. Nevertheless, it was found to be well fitted when compared with the absorbance spectrum of $SrTiO_3/TiO_2$ experimentally obtained (**Figure 2-5**). Ag film was deposited through thermal evaporation process, and nominal thicknesses were controlled to 5 nm and 10 nm to find the position in which the plasmonic absorption of Ag NPs was shown. In the heterostructures before dewetting, broad bands of Ag plasmonic band

appeared at ~ 530 nm at 5 nm thickness and ~ 570 nm at 10 nm thickness (**Figure 2-6**). 5 nm-thick Ag film was selected for the following experiments due to its larger plasmon intensity and easiness to match with structural absorption. In contrast, for 10 nm-thick Ag films, regular deposition was not achieved thus the effective optimization could not be achieved. After dewetting, the absorption was pulled back toward the shorter wavelength because of the blue shift. This is believed to be due to the quantum confinement effect. As steps proceed, the band alignment may not be accurate because the plasmonic absorption band shifted repeatedly.

2.3.3 Photoelectrochemical tests

The photoelectrochemical behaviors of $SrTiO_3/TiO_2$, Ag film/$SrTiO_3/TiO_2$, and Ag NPs(matched)/$SrTiO_3/TiO_2$ were evaluated

by recording the *I-V* characteristics (**Figure 2-7**). *I-V* data were recored with the electrodes in 1 M Na_2SO_4 solution under the irradiation of UV light. The term 'matched' means that the plasmonic absorption and the structural absorption bands were matched or nearly overlapped. UV diffuse reflectance spectra of the heterostructures with matched bands and unmatched bands were presented in **Figure 2-8**. $SrTiO_3/TiO_2$ showed a zero current potential (flat band potential) at ~ -0.37 V vs. NHE. A negative shifts of ~ 50 mV and ~ 80 mV were shown with Ag film/$SrTiO_3/TiO_2$ and Ag NPs(matched)/$SrTiO_3/TiO_2$, resepectively. The flat band potential represents the apparent Fermi level of TNAs in equilibrium with a redox couple.[65] Therefore, the negative shift of zero current potential means that the Fermi level rendered the heterostructure more reductive characters and is indicative of larger accumulation of electrons when irradiated, thus proved the decreased recombination of charge carriers. Not only

$SrTiO_3$ NPs, also Ag NPs were helpful for the additional accumulation of electrons in the heterostructure which would enhance the efficiency of electron harvesting. Ag NPs might played a role for mediating the plasmonic hot-electron generation and band matching with the structural absorption of TNAs.

In **Figure 2-9**, the photocurrent responses of $SrTiO_3/TiO_2$, Ag NPs(unmatched)/$SrTiO_3/TiO_2$, and Ag NPs(matched)/ $SrTiO_3/TiO_2$ were presented. While the response to the illumination was prompt in every electrode, the current density varied upon the existence of Ag NPs and whether the plasmonic and the structural absorption bands were matched or not. The photocurrent density of Ag NPs(matched)/$SrTiO_3/TiO_2$ reached ~10 μA cm^{-2} at the first spike which was 3.6 times and 12.5 times higher than that of Ag NPs(unmatched)/$SrTiO_3/TiO_2$ with ~2.8 μA cm^{-2} and $SrTiO_3/TiO_2$ having not Ag NPs on the surface with ~0.8 μA cm^{-2}. Even after the

degradation of photocurrent which might be attributed to the oxidation of Ag NPs, the current ratio of Ag NPs(matched)/$SrTiO_3$/TiO_2 to Ag NPs(unmatched)/$SrTiO_3$/TiO_2 was maintained its value over 2.5.

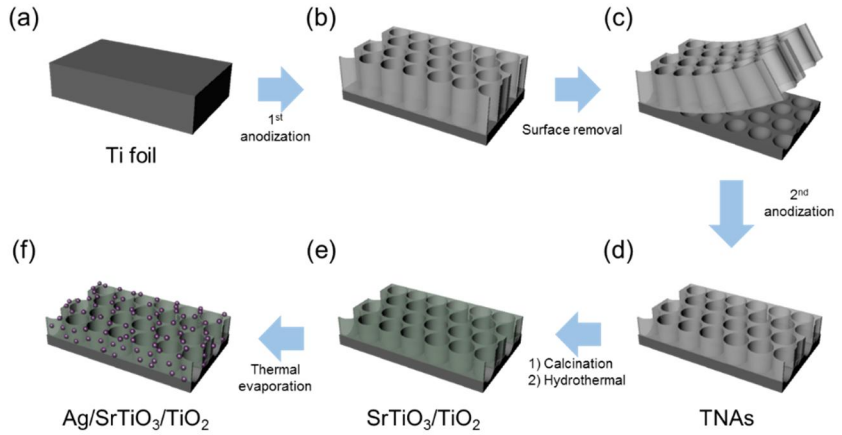

Scheme 2-1. A schematic diagram of the fabrication of Ag/$SrTiO_3$/TiO_2 heterostructures. (a) A Ti foil is prepared as a source of TNAs. (b) TNAs are formed on the Ti foil after the 1st anodization. (c) Top oxide layer is removed by using a tape leaving a pattern on the remaining Ti foil. (d) TNAs with photonic crystal property is formed after the 2nd anodization. (e) $SrTiO_3$/TiO_2 is formed after the calcination followed by the hydrothermal process. (f) Ag NPs are

deposited on the surface by thermal evaporation and dewetting process.

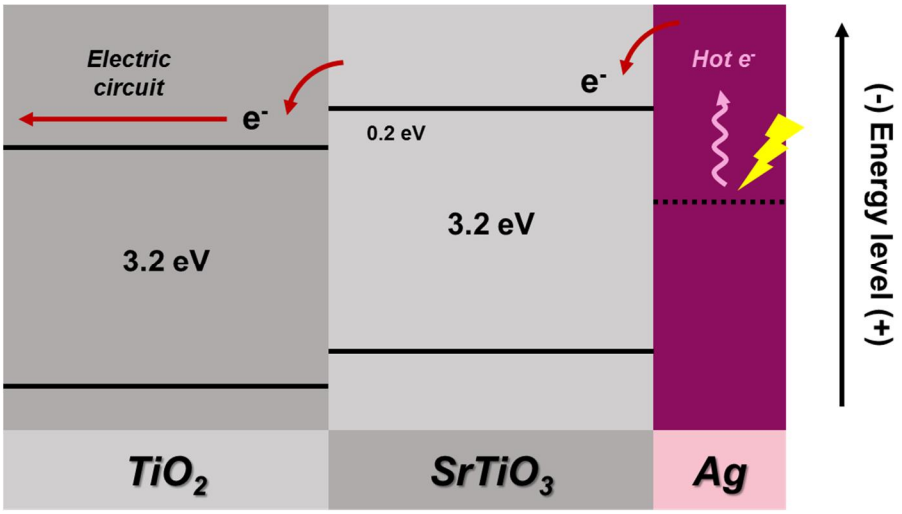

Scheme 2-2. Schematic energy band diagram of $Ag/SrTiO_3/TiO_2$, showing the electron-transfer pathways across the components to be collected into the external circuit. From Ag, plasmon-induced hot electrons are transferred to the CB of $SrTiO_3$ and then to the CB of TiO_2.

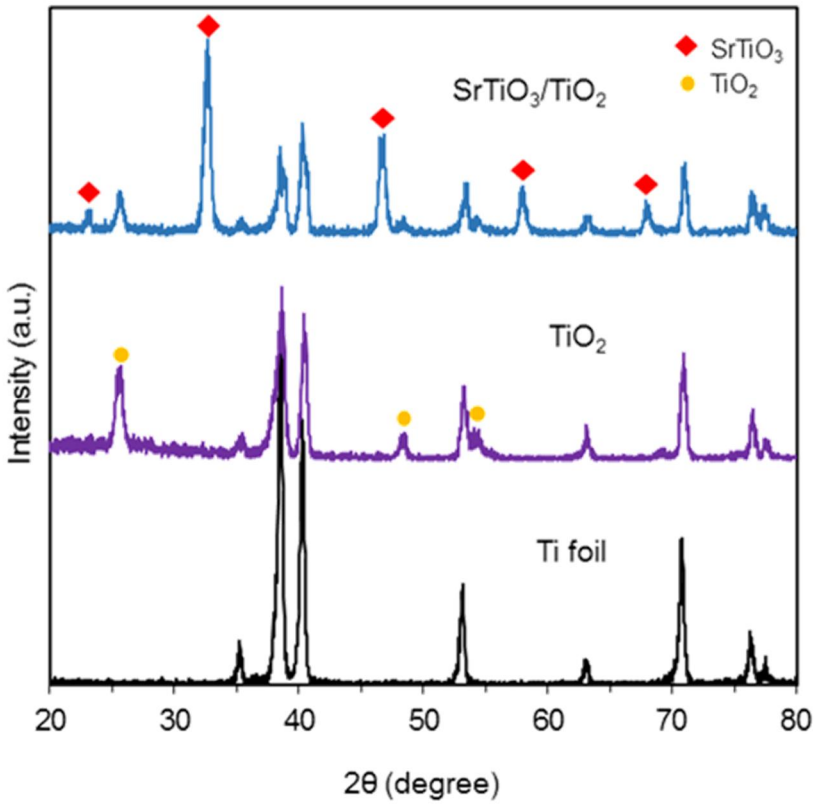

Figure 2-1. X-ray diffraction spectra of Ti foil, TiO_2, and $SrTiO_3/TiO_2$.

TiO_2 indicates the TiO_2 nanotube arrays.

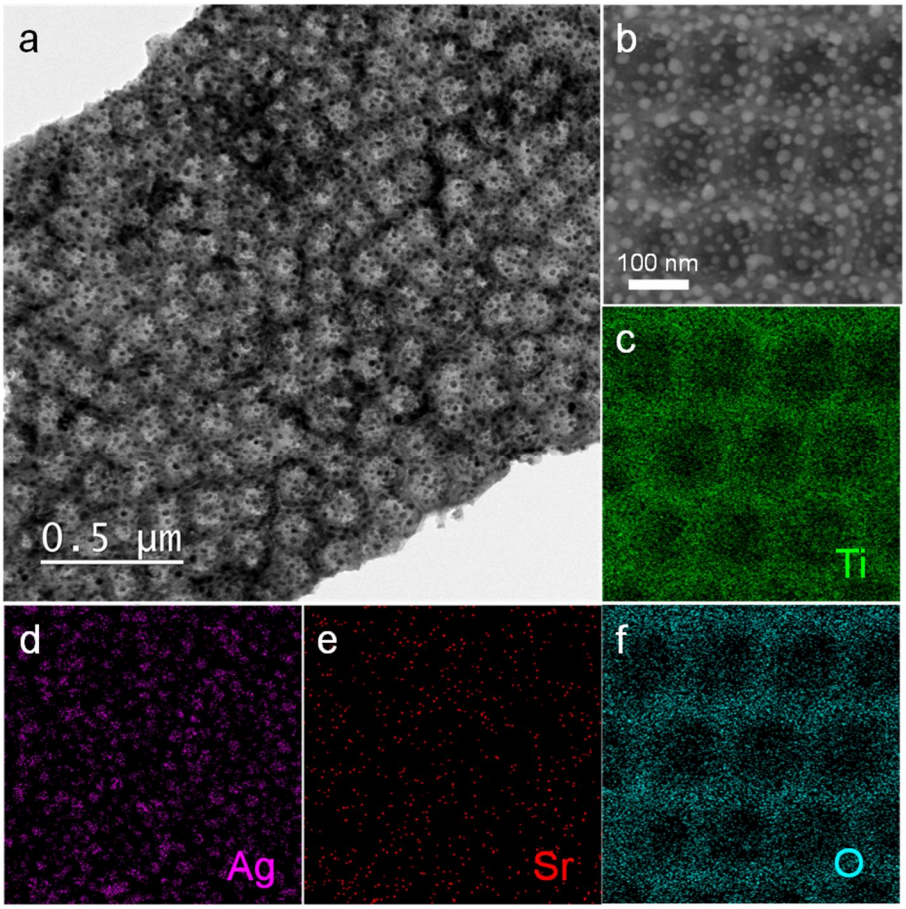

Figure 2-2. Morphology and composition of $Ag/SrTiO_3/TiO_2$ heterostructures using microscopy techniques. (a) STEM image of $Ag/SrTiO_3/TiO_2$. (b) SEM image of $Ag/SrTiO_3/TiO_2$ and (c-f) 2D elemental mapping of Ti, O, Sr, and Ag.

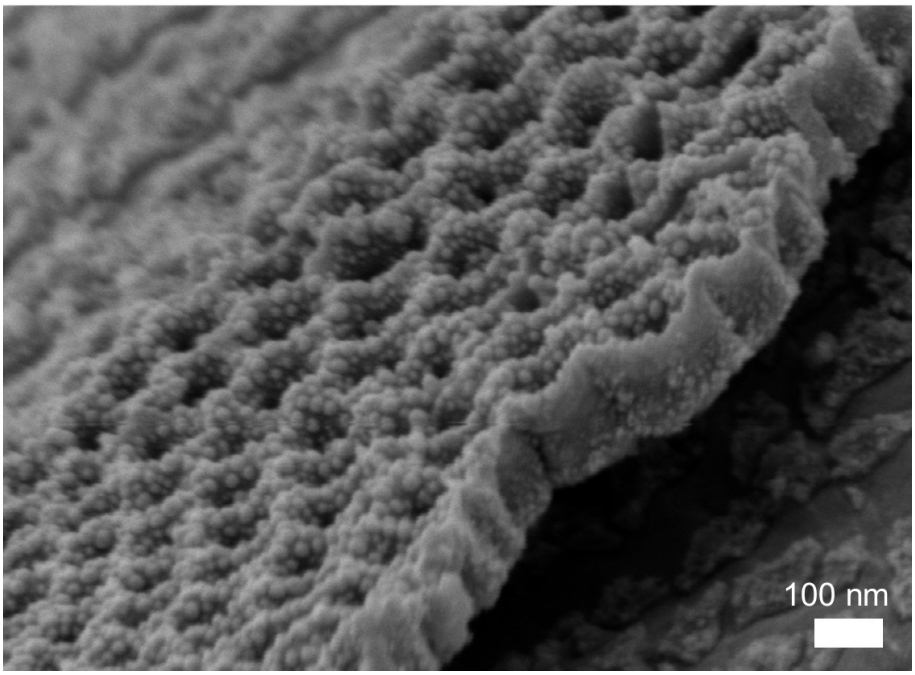

Figure 2-3. Side-view SEM image of $Ag/SrTiO_3/TiO_2$ heterostructure which shows the thickness of the film.

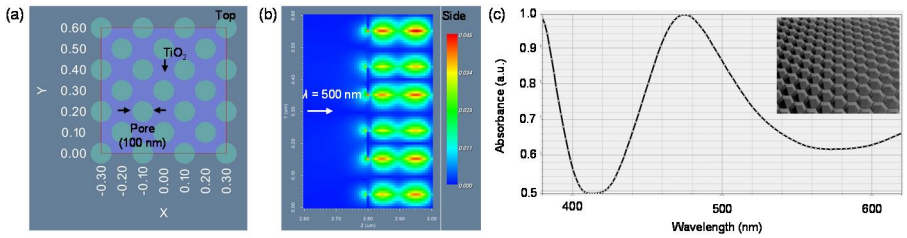

Figure 2-4. (a) Simulation geometry of TiO_2 photonic crystal with a pore diameter of 100 nm. (b) Enhanced electric field at the TiO_2 photonic crystal calculated by FDTD with light wavelengths of 500 nm. (c) Calculated absorption spectrum of the TiO_2 photonic crystal.

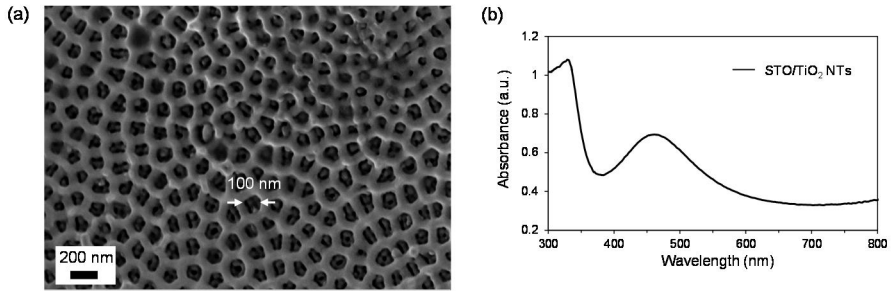

Figure 2-5. (a) SEM image and (b) absorbance spectrum of $SrTiO_3/TiO_2$ photonic heterostructure.

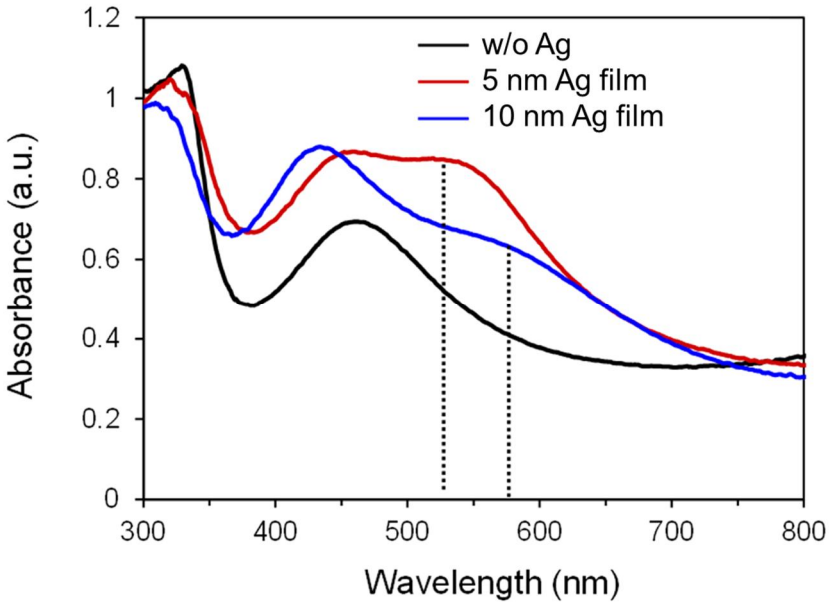

Figure 2-6. UV/vis diffuse reflectance spectra of $SrTiO_3/TiO_2$ heterostructures without Ag, with 5 nm Ag film, and with 10 nm Ag film on the surface.

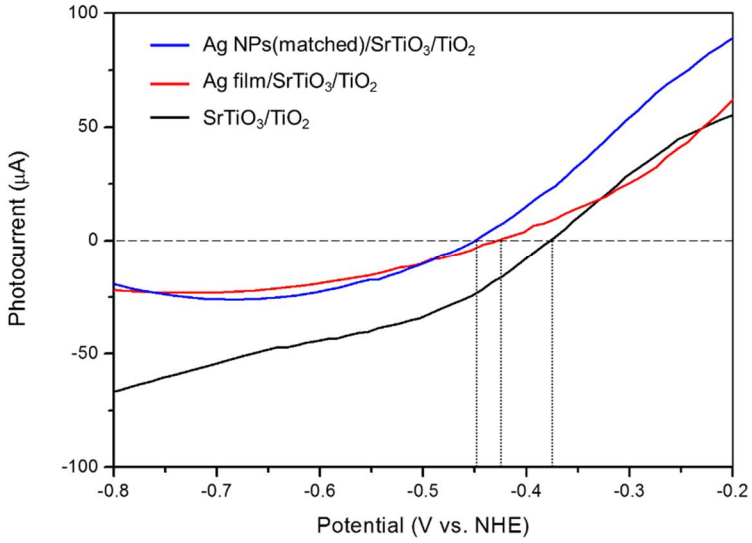

Figure 2-7. *I-V* characteristics of Ag NPs(matched)/$SrTiO_3$/TiO_2, Ag film/$SrTiO_3$/TiO_2, and $SrTiO_3$/TiO_2. (electrolyte = 1 M Na_2SO_4, Pt counter electrode, and under UV light irradiation)

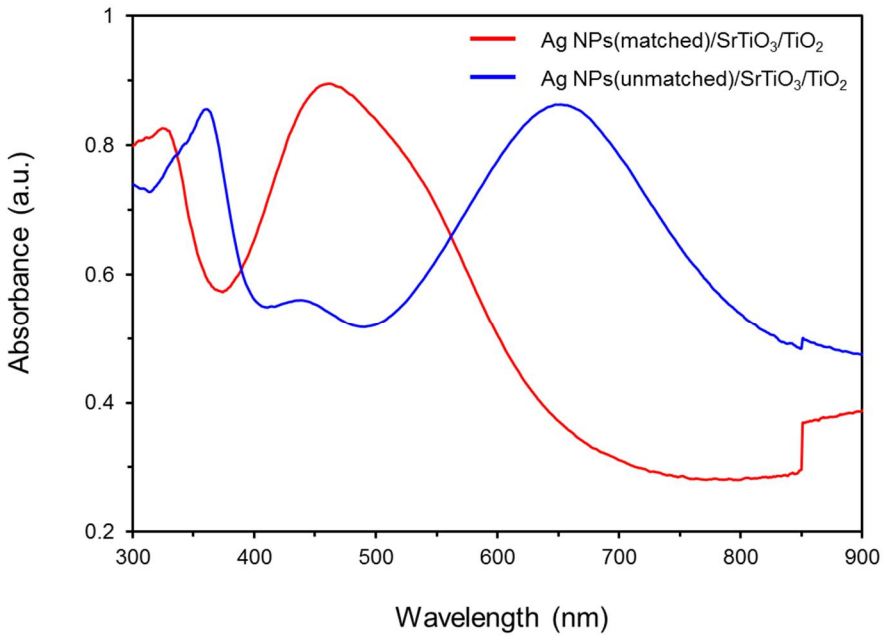

Figure 2-8. UV/vis diffuse reflectance spectra of $SrTiO_3/TiO_2$ heterostructures with Ag NPs(matched) and Ag NPs(unmatched) on the surface.

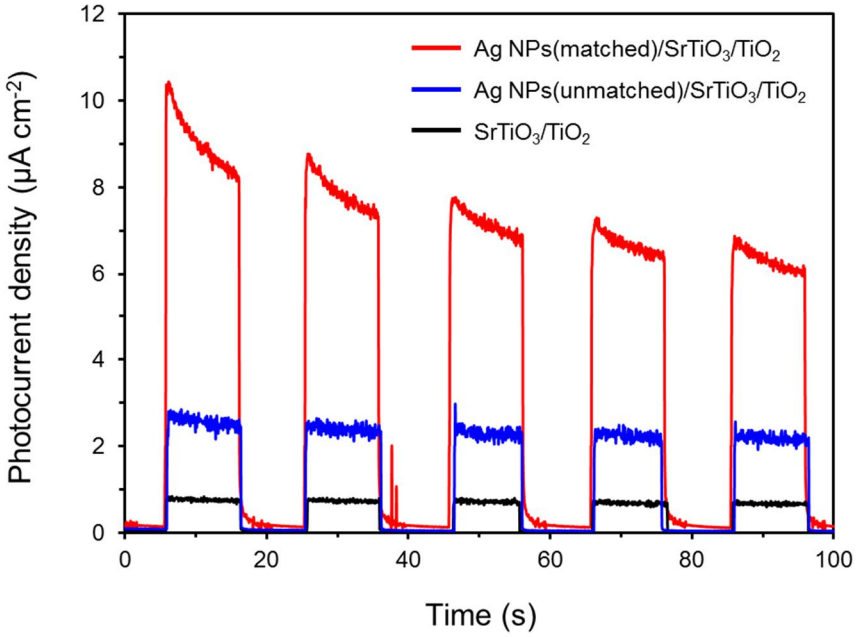

Figure 2-9. Photocurrent density *versus* time measurements of Ag NPs(matched)/$SrTiO_3$/TiO_2, Ag NPs(unmatched)/$SrTiO_3$/TiO_2, and $SrTiO_3$/TiO_2 heterostructures.

Chapter 3. Photocatalytic degradation of acetaldehydes on TiO_2 combined with metal cocatalysts

3.1 Introduction

TiO_2 nanoparticles have been widely used for the photocalytic degradation organic compounds and photoelectrochemical light energy conversion.[10, 26, 32, 66] Because the photogenerated charges are consumed at the surface of photocatalysts by redox reactions, use of metal cocatalysts or surface engineering are required for the optimization of photoexcitation in TiO_2. Metal/TiO_2 composites can enhance the photocatalytic performance by improving the charge separation. It is attributed to the special charge separation and the electric field formed at the interface of TiO_2 and metal.[29, 36] The energy barrier called Schottky barrier is formed at the interface of

n-type semiconductor and metal with a large work function, which facilitate the charge separation.[67]

Modern people live more than 80% of the day in a house or office. Due to air pollutants generated from building materials and heating appliances in an enclosed indoor environment, people suffer various physical/mental health disorders.[68] Thus creating a comfortable indoor environment for people is not only important to increase work efficiency but also to maintain health. Especially, worries against sick building/house syndrome have attracted a great interest, and regulations on indoor building materials and indoor air quality have been strengthened. Since the cause of sick house syndrome is complicated and diverse, it is necessary to seek a fundamental solution to reduce all the harmful substances contained in the indoor environment.[69, 70] One of the representative materials causing the sick house syndrome is an acetaldehyde. Fundamental understanding

on the degradation mechanism or required conditions is needed to effectively remove the gas-phase acetaldehyde.

TiO_2, which is low in manufacturing cost and mass-producible, is currently used as a commercial photocatalyst material. However, the light conversion efficiency is very low because electron-hole pairs generated by the photoexcitation suffer ultra-fast recombination within nanoseconds to picoseconds resulting in slow degradation rate of organic pollutants. Moreover, large bandgap energy of TiO_2 makes it hard to be used under the visible light such as in the indoor environment.

In this study, the importance of metal cocatalysts, especially Pt, is investigated by comparing aqueous and gaseous phase photocatalytic decomposition of acetaldehyde. Fundamental understanding on the role of Pt cocatalyst focusing on the suface adsorption properties is provided. Consequently, the photocatalyst developed in this study has

excellent decomposition ability compared to other commercial products and can be expected to have a constant air purification effect. It has all the requirements for commercialization in terms of color, price competitiveness and performance of photocatalyst. Therefore, based on superiority, it is expected that practical applications such as domestic and automobile interior paint, removal of the chemical odor of the research institute, and removal of odor from the industrial complex.

3.2 Experimental

3.2.1 Preparation of catalysts

Commercial P25 and rutile TiO_2 were used as support TiO_2. For the comparison, bandgap-controlled carbon-doped TiO_2 (C-TiO_2) was synthesized by the hydrothermal sol-gel method and it had an anatase phase. Metal / TiO_2 composites were prepared by the following method. 0.5 g of TiO_2 was added to the reactor containing 150 mL of distilled water. The amount of precursor was calculated and added to the reactor so that the nominal wt% of the metal became 1 wt%. Precursors were dispersed in the aqueous solution by sonicating the solution for 30 minutes. In order to minimize the reduction of metal by light, the aluminum foil was used to wrap the reactor and the pH was adjusted to control the size of nanoparticles. After reaching the target pH, a reducing agent solution containing 0.01 g of $NaBH_4$ dissolved in 15 mL of distilled water was injected dropwise. The solutions were

aged for 3 hours including the reduction time. The temperature was kept constant at 40 °C using a external temperature controller during the injection of the reducing agent to obtain uniform particle size.

3.2.2 Characterization

XRD patterns of the catalysts were measured by using a Rigaku d-MAX2500-PC powder X-ray diffractometer operating at 50 kV and 100 mA using Cu-Kα radiation (1.54 Å). High-resolution transmission electron micrograph (HR-TEM) images were obtained on JEOL JEM-3010 microscope with an acceleration voltage of 300 kV. The N_2 physisorption were carried out on a Micrometrics ASAP-2010 system and the total surface area of the samples was calculated by the BET method (P/P_o=0.05~0.15). X-ray photoelectron spectroscopy (XPS) was performed with a Sigma Probe instrument (ThermoVG). The binding energy of each element was calibrated by using the carbon

peak as standard (C 1s = 284.5 eV). Optical absorpbance were investigated by ultraviolet-visible diffuse reflectance spectroscopy (UV-DRS, V670-Jasco) with BaSO4 as a reference. Fourier transform infrared (FT-IR) spectra were obtained by using Bruker Tensor27 to investigate the adsorption of acetaldehydes. Wavenumber scan range was 4000 ~ 1000 cm^{-1}. Temperature programmed desorption (TPD) profiles of acetaldehyde and water were obtained by recording the signals of mass spectrometer graph connected to the gas-phase catalyst reactor. The pre-treatment of the catalysts were achieved at 300 ^{o}C. Temperature ranges were 50 ~ 400 ^{o}C for acetaldehyde desorption, and 110 ~ 400 ^{o}C for water desorption.

3.2.3 Photocatalytic degradation of acetaldehydes

For the comparison with commercial photocatalysts, gas-phase acetaldehyde degradation tests were conducted under the LED light. The photo and specral information of the LED are shown in **Figure 3-1**. Tests were performed in the homemade reactor system (**Figure 3-2**). The aqueous solution of acealdehyde was evaporated and diluted by flowing with hot air. In the reactor system, flow rate of gases was controlled to 50 mL/min by a circulation pump and the volume of photoreactor was 277 mL. Concentration of acetaldehyde in the reactor was measured by gas chromatography equipped with a flame ionization detector (GC-FID) periodically. The temperature of photoreactor was maintained to 40 ^{o}C using an external temperature controller. For the investigation of surface properties of Au/TiO_2 and Pt/TiO_2, photocatalytic activity tests were conducted under UV light

or visible light ($\lambda > 400$ nm) using a 300 W Xe lamp as a source. Photocatalysts were prepared as a paste by doctorblading method on a PVC substrate. 0.15 g of catalyst was used in each test. Commercial photocatalysts used in this study are as follows:

(1) P25 (provider: Degussa)

(2) Japan catalyst 1 (JC-1) (provider: confidential, Japan)

(3) Japan catalyst 2 (JC-2) (provider: confidential, Japan)

To test the reliability of experimental results and commercial competitiveness, the performance of acetaldehyde decomposition of prepared catalysts were evaluated by Korea Conformity Laboratories (KCL). In KCL, used light sources were two OSRAM FL20SSEX-D/18 and the catalysts were pre-treated and coated on 10 cm × 10 cm substrate then tested for two hours. Concentration in the gas phase was detected by GASTEC GV-100.

3.3 Results and discussion

3.3.1 Catalyst characterization

JC-1 and JC-2 showed the crystalline phase of rutile TiO_2 and has a bandgap of 3.0 eV without any absorption in the visible light region (**Figure 3-3 and Figure 3-4(a)**). While they include Pt and Fe-containing metal nanoparticles respectively, any peaks were not observed in XRD spectra because of the low concentration and high crystallinity of TiO_2. JC-1 consisted of TiO_2 nanoparticles of 30 ~ 80 nm size and JC-2 consisted of rod-like TiO_2 nanoparticles of 50 ~ 200 nm size (**Figure 3-5(a,b)**). C-TiO_2 consisted of an anatase phase and showed a significant absorption in the visible light region. The morphology and UV/vis spectrm of Pt/P25 was also investigated. With nominal 1 wt% of Pt on P25, Pt nanoparticles of 2 ~ 4 nm size were

deposited on TiO_2 nanoparticles on 30 ~ 50 nm size and it showed absorption over the range of visible light (**Figure 3-4(b), Figure 3-5(c,d)**). UV/vis diffuse reflectance spectra of prepared catalysts for the surface adsorption study, 1 wt% Au/TiO_2 and 1 wt% Pt/TiO_2, were presented in **Figure 3-6**. It is notable that Au/TiO_2 shows the plasmonic absorption at the wavelength of 550 nm. The surface area of the catalysts were measured by BET analysis and metal deposition did not affect the specfic surface area (**Table 3-1**).

3.3.2 Photocatalytic activity tests

For the comparison, the photocatalytic performances of commercial photocatalysts and bandgap-controlled carbon doped TiO_2 (C-TiO_2) were investigated for 10 ppm methylene blue (MB) solutions (**Figure 3-7(a)**). Under the visible light irradiation ($\lambda > 400$ nm), the activity of

C-TiO_2 was superior to the other catalysts. This is due to the enhanced visible light absorption of C-TiO_2 originated from the controlled bandgap energy from 3.2 eV to 2.4 eV. In aqueous phase, the rate constant for MB degradation of C-TiO_2 was 2.7 times higher than JC-1 (**Table 3-2**) However, this trend was not reproduced in the gas-phase acealdehyde degradation. In contrast to the MB degradation results, C-TiO_2 was not effective than JC-1 (**Figure 3-7(b)**). This might be attributed to the hydrophobic surface of C-TiO_2 which hinders the formation of ·OH radicals for organic degradation even C-TiO_2 absorbs the light better.

In particular, JC-2 and JC-2 in paint adsorbed a significant amount of MB in the adsorption equilibrium tests and the rate of MB degradation were relatively low (**Figure 3-8**). The results show that the photocatalytic performance of JC-2 was mainly attributed to absorption not from the degradation power.

Several noble metals, such as Pd, Ag, and Pt, were combined with P25 catalyst to screen the metal cocatalysts for acetaldehyde degradation. As shown in **Figure 3-9** and **Table 3-3**, Pt was the best cocatalyst among Pd, Ag, and Pt. 1 wt% Pt/P25 showed outstanding performance with 2.21 times higher degradation rate than JC-1 which showed the best performance among the commercial photocatalysts. This indicated the excellence of Pt as a cocatalyst for acetaldehyde degradation and it was also evaluated by KCL (**Table 3-4**). In order to optimize the amount of Pt, weight percent of Pt was controlled in the range of 0.1 ~ 0.3 wt% and pH was adjusted to control the size and dispersion of nanoparticles. The results is shown in **Table 3-5**. Further investigations are required to understand the role of size and dispersion.

3.3.3 Investigations on surface adsorption of acetaldehyde

To investigate the surface adsorption properties of acetaldehyde, bare TiO_2, 1 wt% Au/TiO_2, and 1 wt% Pt/TiO_2 were compared as representatives. Rutile TiO_2 was used as a support in the study. It is not difficult to understand that the performance is higher as catalysts are irradiated and the surface concentration of water and oxygen is sufficient for the reaction. In **Figure 3-10**, photocatalytic acetaldehyde degradation results of the catalysts are presented. The results show that the activity of Pt/TiO_2 was almost the same in both humid and dry conditions. Dry condition means that the reactant acetaldehyde was not injected through the aqueous solution. In contrast, degradation rates of bare and Au/TiO_2 became faster in dry condition rather than in humid condition. It is known that the surface adsorbed water plays a key role to generate ·OH radicals thus improving the degradation rate

of organic pollutants. However, the results were contradictory to this fact that indicate the reaction proceed when acetaldehyde is adsorbed on the surface in competition with water. The spikes at the beginning of degradation might come from the temporary concentration increase due to the surface adsorption of water.

TPD results were presented in **Figure 3-11**. After the pretreatment at 300 ^{o}C, the desorption of acetaldehyde was investigated in the temperature range of 50 ~ 400 ^{o}C. Ramping rate was 10 K/min. There usually exists two kinds of adsorption of acetaldehyde. In **Figure 3-11 (b)**, the first peak comes from the weak hydrogen bond with surface hydroxyl groups and the second peak comes from the strong chemical adsorption to the surface of TiO_2.[71] The result indicated that acetaldehyde forms strong bonds with Pt/TiO_2 so that Pt/TiO_2 was not affected by the concentration of water. In Au/TiO_2, acetaldehyde competes with water on the surface so that it is sensitive to the

concentration of water. Moreover, an additional peak between the previous two peaks emerged and the peak might come from the new type of bond between acetaldehyde and Pt. Infrared spectra provide a clue of the additional type of bond formation (**Figure 3-12**). It is notable that the reverse peaks were emerged back and forth 2900 cm^{-1} which correspond to π-bonding of acetaldehyde on Pt metal.[72] This type of new bonds make acetaldehyde more fixable on the surface of Pt/TiO_2 so as to assist the strong chemical bond with Pt/TiO_2 as also shown in the TPD results. As a result, the enhanced degradation of acetaldehydes on Pt/TiO_2 might be attributed to Pt-induced strong adsorption of acetaldehydes on the surface of TiO_2 as presented in **Figure 3-13**. It is also supported by the well-known oxophilic character of Pt nanoparticles.

Table 3-1. Specific surface area of TiO_2, Au/TiO_2, and Pt/TiO_2 measured by BET analysis.

	BET surface area (m^2 g^{-1})
TiO_2	38.2992
Au/TiO_2	43.1233
Pt/TiO_2	43.1581

Table 3-2. Rate constants for photocatalytic MB degradation of JC-2, P25, JC-1, and C-TiO_2.

Sample	Rate constant (h^{-1})	Ratio
JC-2	0.0121	1
P25	0.0258	2
JC-1	0.2031	17
C-TiO_2	0.5568	46

Table 3-3. Rate constants for photocatalytic acetaldehyde degradation of JC-1, P25, 1Ag/P25, 1Pd/P25, and 1Pt/P25. The number '1' as a prefix indicates the nominal weight percent of metals were 1 wt%.

Sample	Rate constant (h^{-1})	Ratio
JC-1	0.4882	1
P25	0.0837	0.17
1Ag/P25	0.2450	0.50
1Pd/P25	0.0296	0.06
1Pt/P25	1.0793	2.21

Table 3-4. KCL evaluation results of JC-1 and 1Pt/P25.

Sample	Cocatalyst	Support	Color	KCL evaluation
JC-1	Pt (0.6~0.7%)	TiO_2	White	100%
1Pt/P25	Pt (1.0%)	TiO_2	Gray	100%

Table 3-5. KCL evaluation results of Pt/TiO_2 catalysts with different amount of Pt cocatalyst and synthetic conditions.

Sample	Cocatalyst (wt%)	pH, calcination Temperature (°C)	Color	KCL evaluation
Pt/TiO_2	~0.1%	pH 1, 300	White	100
Pt/TiO_2	~0.1%	pH 2, 300	White	100
Pt/TiO_2	~0.1%	pH 3, 300	White	94
Pt/TiO_2	~0.2%	pH 1, 300	White	100
Pt/TiO_2	~0.3%	pH 1, 300	White	95

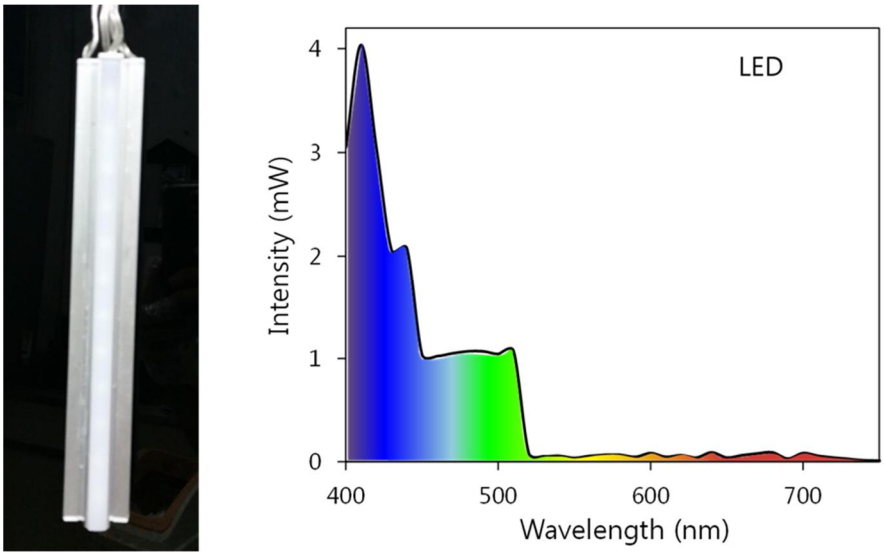

Figure 3-1. LED lamp used in the homemade photocatalytic reactor system and the measured spectral information of lamp.

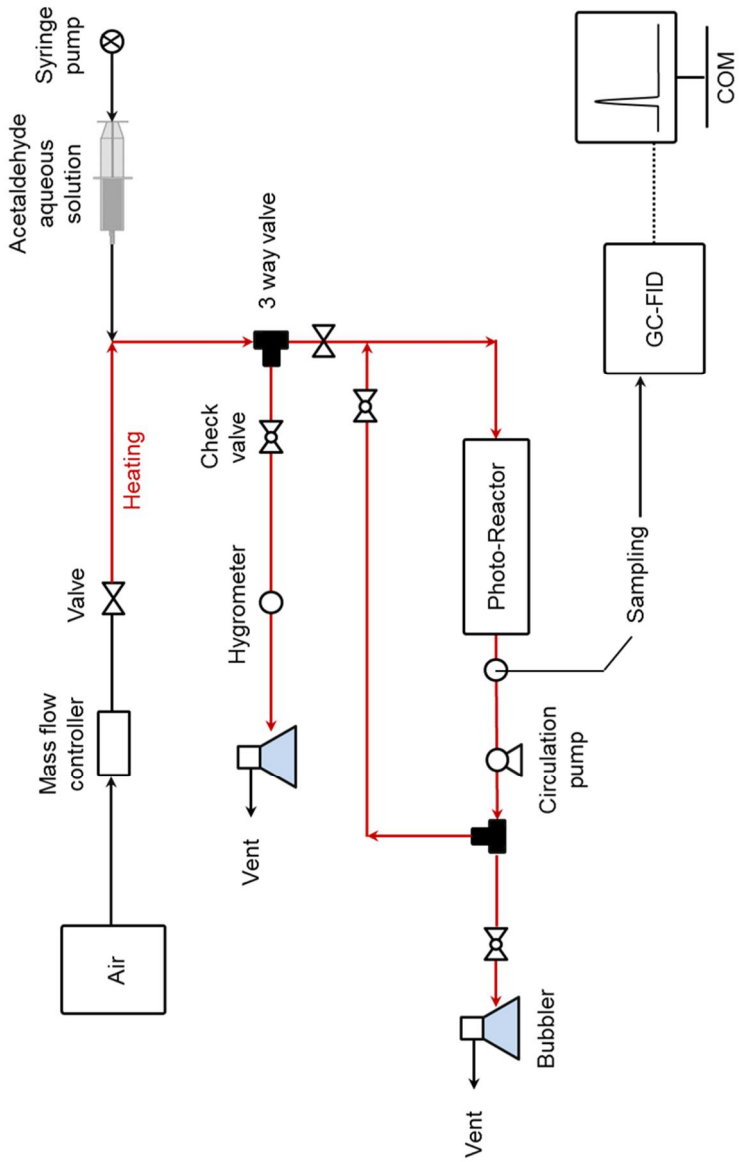

Figure 3-2. A mimetic diagram of the homemade photocatalytic reactor system for gas-phase acetaldehyde degradation.

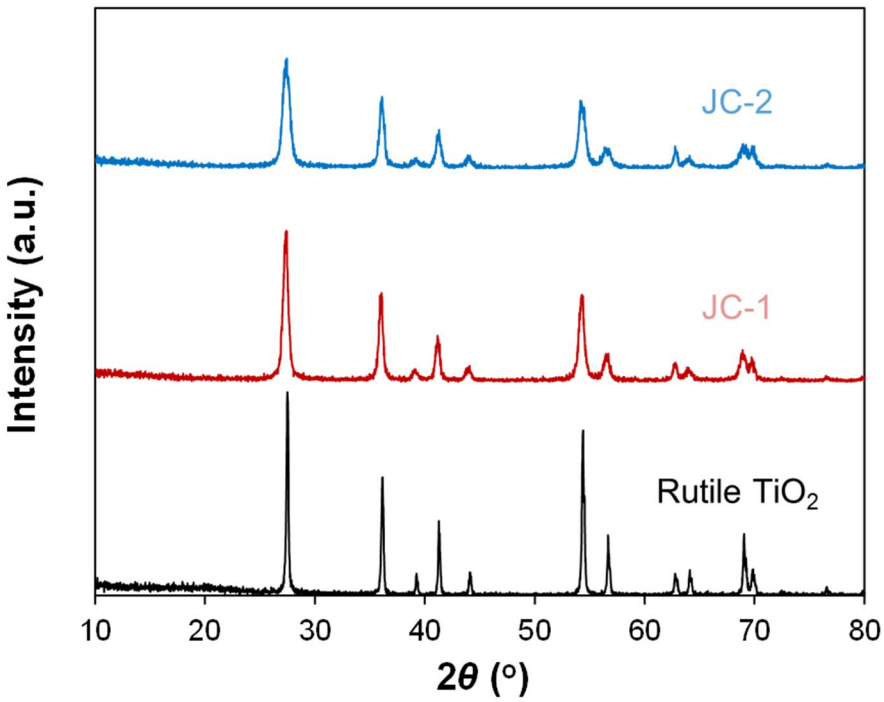

Figure 3-3. X-ray diffraction spectra of JC-2, JC-1, and rutile TiO_2.

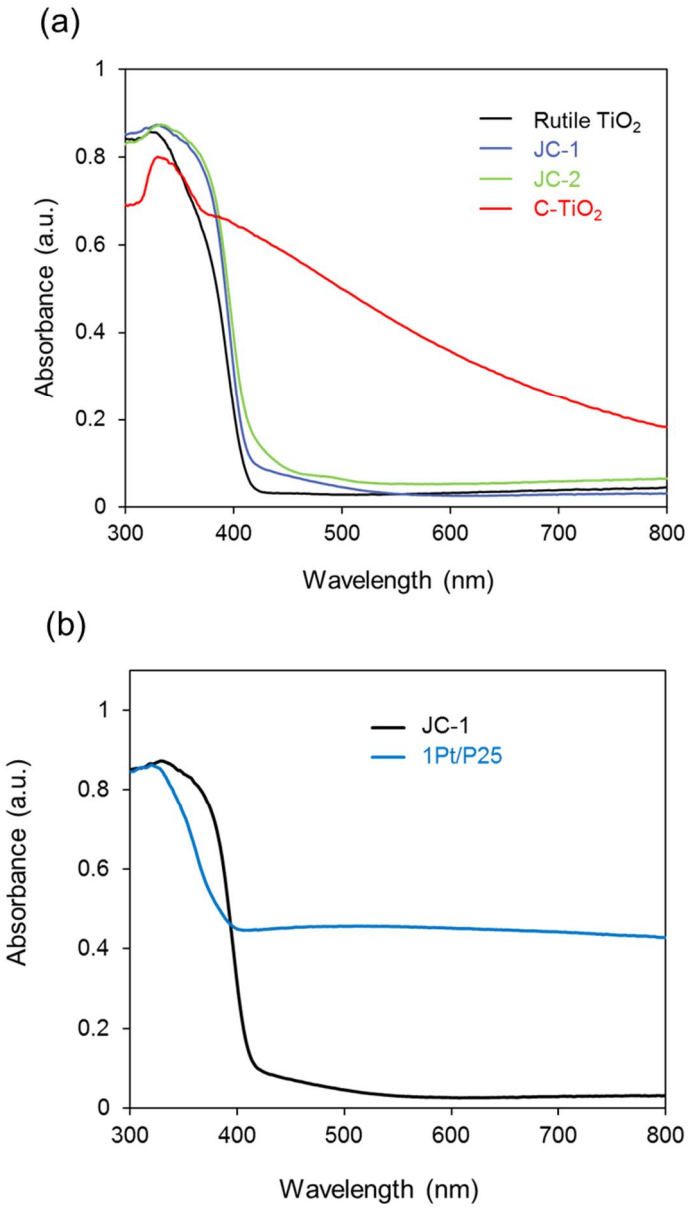

Figure 3-4. UV/vis diffuse reflectance spectra of (a) rutile TiO_2, JC-1, JC-2, C-TiO_2 and (b) JC-1, 1Pt/P25.

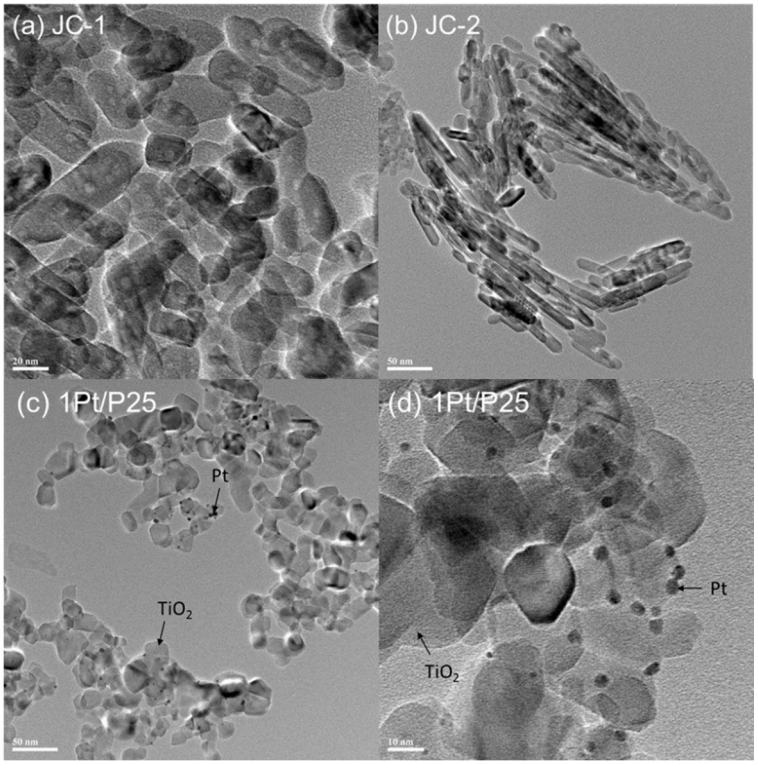

Figure 3-5. TEM images of (a) JC-1, (b) JC-2, and (c, d) 1Pt/P25.

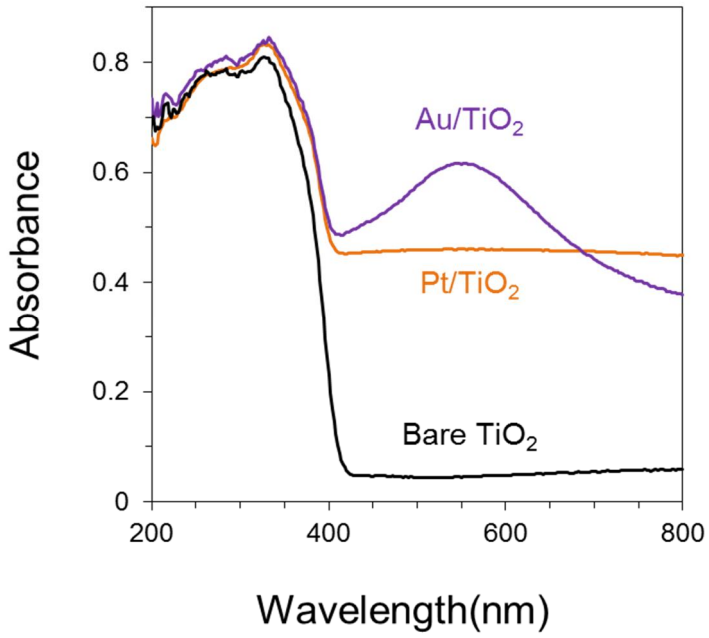

Figure 3-6. UV/diffuse reflectance spectra of bare TiO_2, Pt/TiO_2, and Au/TiO_2.

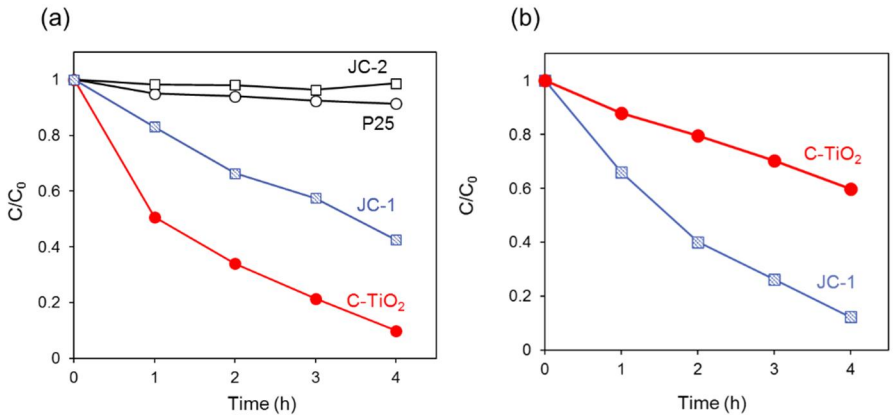

Figure 3-7. C/C_0 plot *vs.* time for (a) aqueous MB degradation of JC-2, P25, JC-1, and C-TiO_2, and (b) gas-phase acetaldehyde degradation of JC-1 and C-TiO_2 under the visible light irradiation ($\lambda > 400$ nm).

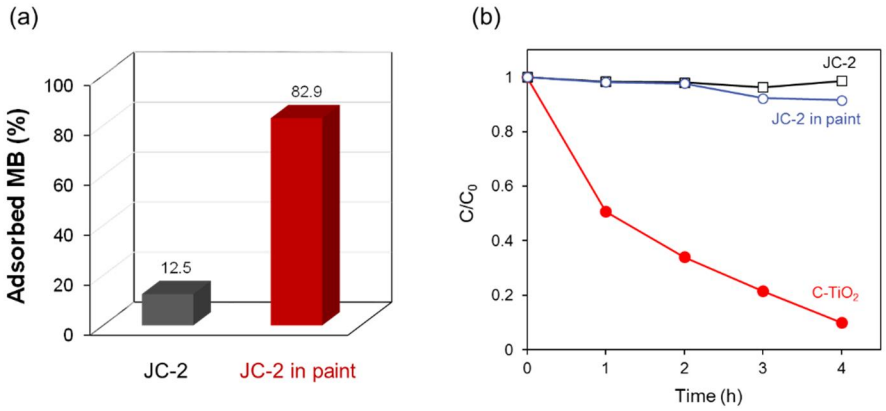

Figure 3-8. (a) MB adsorption equilibrium tests of JC-2 and JC-2 in paint, and (b) C/C_0 plot *vs.* time for MB degradation of JC-2, JC-2 in paint, and C-TiO_2 under the visible light irradiation ($\lambda > 400$ nm).

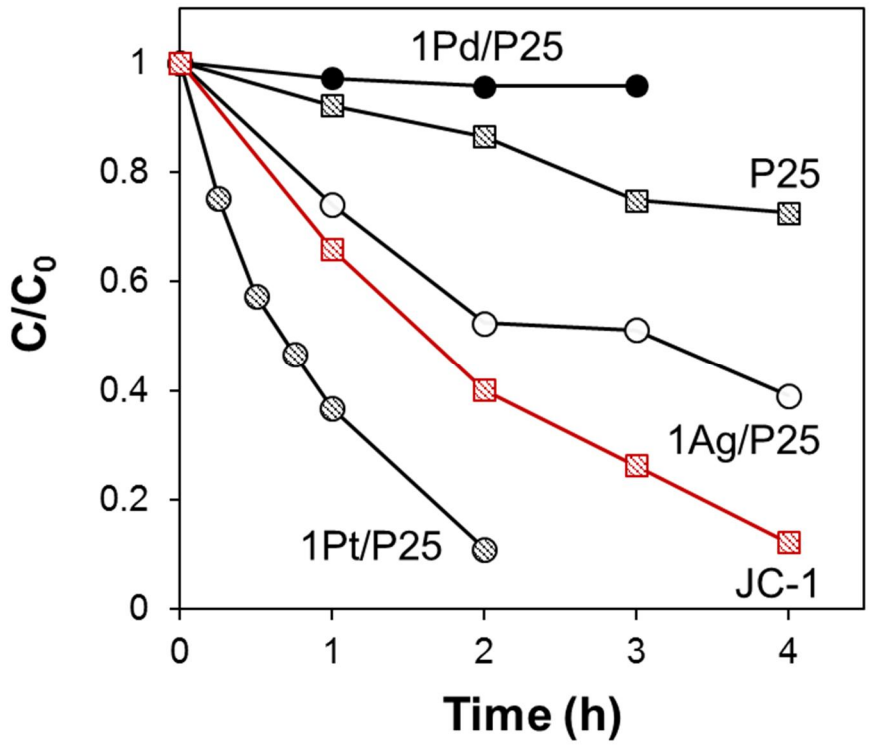

Figure 3-9. C/C_0 plot *vs.* time for gas-phase acetaldehyde degradation of 1Pd/P25, P25, 1Ag/P25, JC-1, and 1Pt/P25 under the visible light irradiation ($\lambda > 400$ nm).

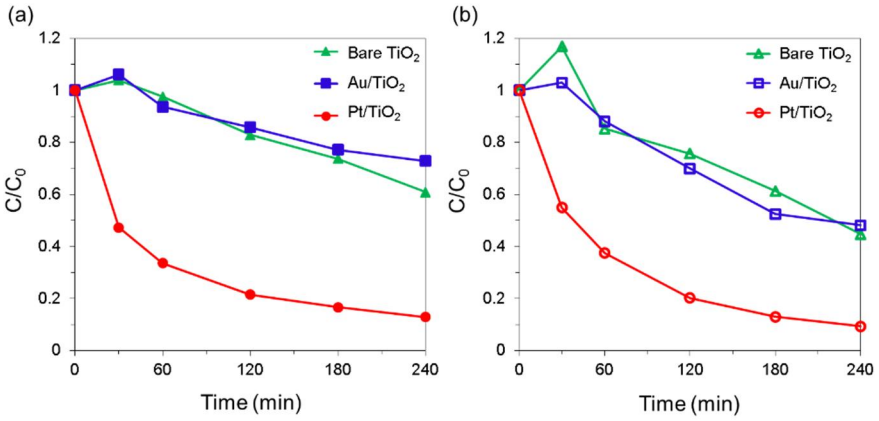

Figure 3-10. C/C_0 plot *vs.* time for gas-phase acetaldehyde degradation of bare TiO_2, Au/TiO_2 and Pt/TiO_2 under the UV light irradiation.

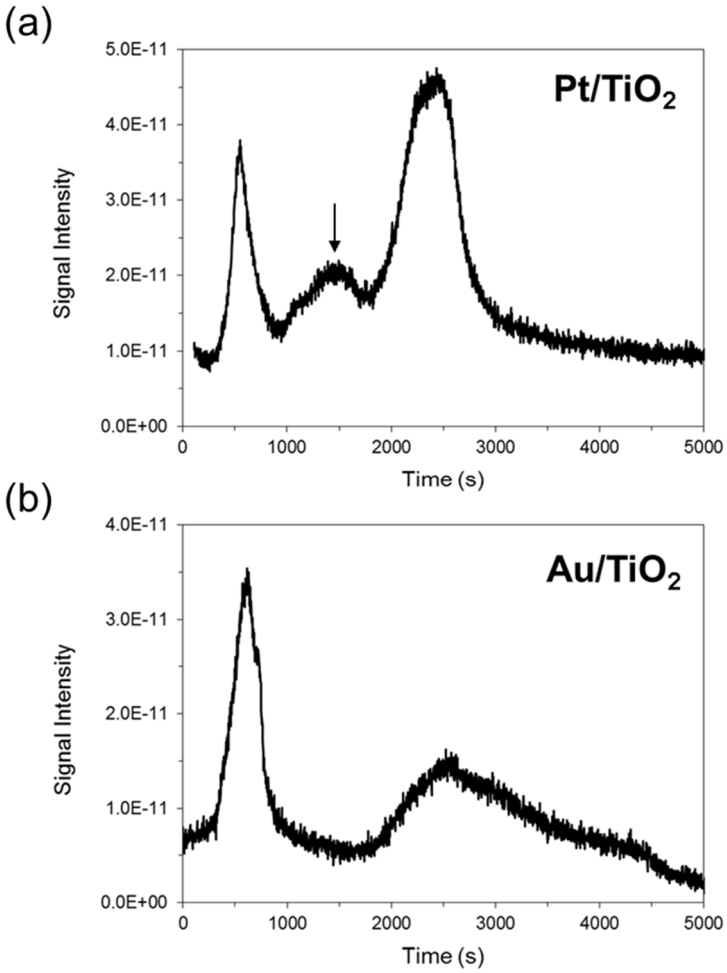

Figure 3-11. TPD profiles of acetaldehyde on (a) Pt/TiO_2 and (b) Au/TiO_2 under dry N_2 flow. The ramping rate was 10 K/min.

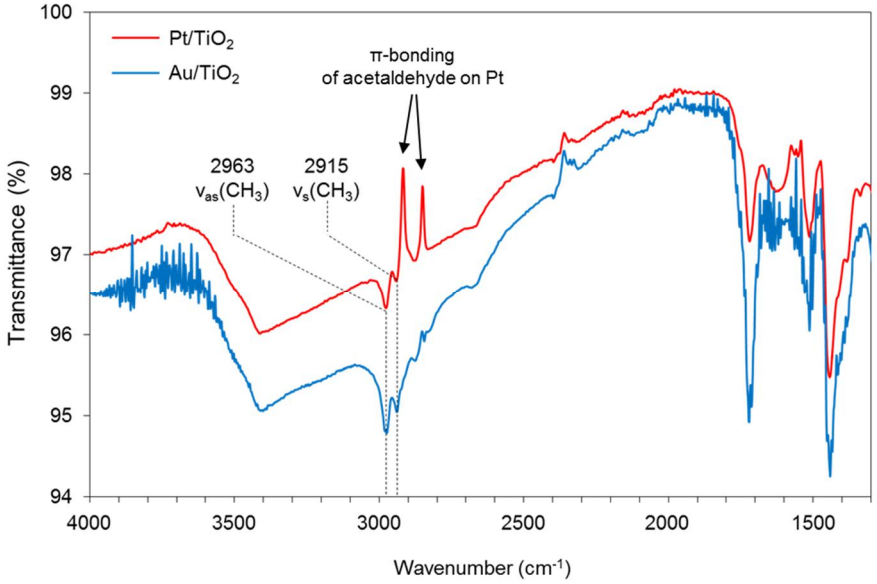

Figure 3-12. FT-IR spectra of Au/TiO_2 and Pt/TiO_2 after the adsorption of acetaldehyde.

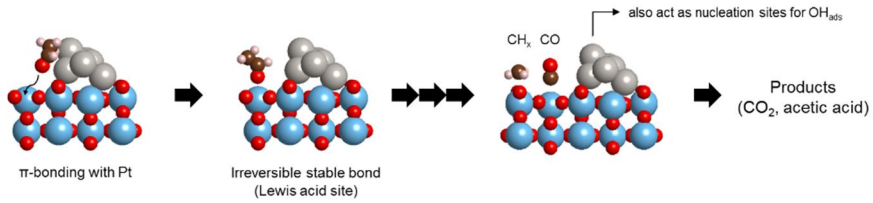

Figure 3-13. Proposed mechanism of acetaldehyde degradation on Pt/TiO_2 considering the role of Pt cocatalyst as a strong-adsorption mediator.

Chapter 4. Summary and Perspectives

TiO_2 nanostructures were exploited to provide the ways how to optimize the utilization of photogenerated charges for electric energy or other photocatalytic reactions. A novel three-component light harvesting system was developed based on TiO_2 nanotube arrays (TNAs) with photonic crystal properties. By combining TNAs with $SrTiO_3$ nanoparticles, TNAs showed higher apparent Fermi level, which means the improved charge separation thus assisting the charge transfer to the external circuit. Moreover, the structural absorption of TNAs was matched with the plasmonic absorption of surface deposited Ag nanoparticles. FDTD method was utilized to optimize the absorption of TNA by tuning the pore depth and diameter. The structural property was characterized by scanning transmission electron microscopy (STEM), scanning electron microscopy (SEM)

and energy dispersive X-ray spectroscopy (EDS). The developed heterostructure (Ag NPs(matched)/$SrTiO_3$/TiO_2) presented the enhanced photocurrent response which were ~ 10 times and ~ 3 times higher compared with $SrTiO_3$/TiO_2 and Ag NPs(unmatched)/$SrTiO_3$/TiO_2. It is expected that this type of PEC system would provide a clue toward development of industrial energy conversion devices, such as photo-induced fuel cell system. Also, this research highlights the importance of support material with tunable wavelength-specific absorption for the efficient light energy conversion.

TiO_2 nanoparticles combined with metal cocatalysts were used to optimize the performance of gas-phase acetaldehyde degradation. Metal cocatalysts usually play a role as an electron sink thus improving the charge separation. Even though the noble metals form similar Schottky junctions with n-type TiO_2 materials due to their

large work functions, photocatalytic performance is not only affected by the improved charge separation but also by other factors such as surface properties and types of cocatalysts. The importance of cocatalysts, especially Pt in gas-phase acetaldehyde degradation, was highlighted in the study by comparing with the commercialized photocatalysts. Moreover, the economic and industrial feasibility was ensured by reducing the required amount of Pt and being accredited by the external evaluation organization. Fundamental investigations focusing on the surface adsorption properties by TPD and FT-IR were tried to understand the role of Pt cocatalyst. The results highlight the importance of appropriate use of cocatalysts and surface engineering for the targeted photocatalytic reaction.

Development of novel TiO_2 nanostructures and combinations with other structural or electronic compartments would present visions for the future sustainable society by providing new strategies for utilizing

the infinite solar energy. Further systematic studies are required with these methods for optimization of photoexcitation to expand the prospects to realize the vision.

Bibliography

1. E.M. Michael, S.B. Raymond, and K.H. Malcolm, *Nature*, **1998**, 392, 779-787.
2. P.V. Kamat, *J. Phys. Chem. C*, **2007**, 111, 2834-2860.
3. G.W. Crabtree and N.S. Lewis, *Physics Today*, **2007**, 60, 37-42.
4. *Key world energy statistics*, I.E. Agency, **2018**.
5. M.R. Hoffmann, S.T. Martin, W. Choi, and D.W. Bahnemann, *Chem. Rev.*, **1995**, 95, 69-96.
6. A. Fujishima, X. Zhang, and D. Tryk, *Int. J. Hydrog. Energy*, **2007**, 32, 2664-2672.
7. K. Nakata and A. Fujishima, *J. Photochem. Photobiol. C-Photochem. Rev.*, **2012**, 13, 169-189.
8. U. Bach, D. Lupo, P. Comte, J.E. Moser, F. Weissortel, J. Salbeck, H. Spreitzer, and M. Gratzel, *Nature*, **1998**, 395, 583-585.
9. K. Hara, H. Sugihara, Y. Tachibana, A. Islam, M. Yanagida, K. Sayama, H. Arakawa, G. Fujihashi, T. Horiguchi, and T. Kinoshita, *Langmuir*, **2001**, 17, 5992-5999.
10. A.-W. Xu, Y. Gao, and H.-Q. Liu, *J. Catal.*, **2002**, 207, 151-157.
11. G.K. Mor, K. Shankar, M. Paulose, O.K. Varghese, and C.A. Grimes, *Nano Lett.*, **2006**, 6, 215-218.
12. J.H. Park, S. Kim, and A.J. Bard, *Nano Lett.*, **2006**, 6, 24-28.
13. J.M. Macak, M. Zlamal, J. Krysa, and P. Schmuki, *Small*, **2007**, 3, 300-304.
14. A. Ghicov, S.P. Albu, R. Hahn, D. Kim, T. Stergiopoulos, J. Kunze, C.A. Schiller, P. Falaras, and P. Schmuki, *Chem.-Asian J.*, **2009**, 4,

520-525.

15. B. Liu, K. Nakata, M. Sakai, H. Saito, T. Ochiai, T. Murakami, K. Takagi, and A. Fujishima, *Langmuir*, **2011**, 27, 8500-8508.
16. K. Nakata, B. Liu, Y. Ishikawa, M. Sakai, H. Saito, T. Ochiai, H. Sakai, T. Murakami, M. Abe, K. Takagi, and A. Fujishima, *Chemistry Letters*, **2011**, 40, 1107-1109.
17. F. Eric, L. Eric, C. Dean, and X. Younan, *Nano Lett.*, **2008**, 8, 668-672.
18. G.L. Chiarello, A. Zuliani, D. Ceresoli, R. Martinazzo, and E. Selli, *ACS Catal.*, **2016**, 6, 1345-1353.
19. K. Katsumata, S. Okazaki, C.E. Cordonier, T. Shichi, T. Sasaki, and A. Fujishima, *ACS Appl. Mater. Interfaces*, **2010**, 2, 1236-1241.
20. W. Guo, F. Zhang, C. Lin, and Z.L. Wang, *Adv. Mater.*, **2012**, 24, 4761-4764.
21. D.O. Scanlon, C.W. Dunnill, J. Buckeridge, S.A. Shevlin, A.J. Logsdail, S.M. Woodley, C.R. Catlow, M.J. Powell, R.G. Palgrave, I.P. Parkin, G.W. Watson, T.W. Keal, P. Sherwood, A. Walsh, and A.A. Sokol, *Nat. Mater.*, **2013**, 12, 798-801.
22. H. Irie, Y. Watanabe, and K. Hashimoto, *Chem. Lett.*, **2003**, 32, 772-773.
23. L. Etgar, P. Gao, Z. Xue, Q. Peng, A.K. Chandiran, B. Liu, M.K. Nazeeruddin, and M. Gratzel, *J. Am. Chem. Soc.*, **2012**, 134, 17396-17399.
24. Y. Bessekhouad, D. Robert, and J.V. Weber, *J. Photochem. Photobiol., A*, **2004**, 163, 569-580.
25. Y. Bessekhouad, N. Chaoui, M. Trzpit, N. Ghazzal, D. Robert, and

J.V. Weber, *J. Photochem. Photobiol., A*, **2006**, 183, 218-224.

26. T. Ohno, T. Mitsui, and M. M., *Chem. Lett.*, **2003**, 32, 364-365.
27. X. Chem and C. Burda, *J. Am. Chem. Soc.*, **2008**, 130, 5018-5019.
28. X. Zhang, Y.L. Chen, R.S. Liu, and D.P. Tsai, *Rep. Prog. Phys.*, **2013**, 76, 046401.
29. J. Schneider, M. Matsuoka, M. Takeuchi, J. Zhang, Y. Horiuchi, M. Anpo, and D.W. Bahnemann, *Chem. Rev.*, **2014**, 114, 9919-9986.
30. E. Bae and W. Choi, *Environ. Sci. Technol.*, **2003**, 37, 147-152.
31. F. Xiao, *J. Phys. Chem. C*, **2012**, 116, 16487-16498.
32. F.B. Li and X.Z. Li, *Chemosphere*, **2002**, 48, 1103-1111.
33. A. Galinska and J. Walendziewski, *Energy Fuels*, **2005**, 19, 1143-1147.
34. H. Li, Z. Bian, J. Zhu, Y. Huo, H. Li, and Y. Lu, *J. Am. Chem. Soc.*, **2007**, 129, 4538-4539.
35. M. Bowker, D. James, P. Stone, R. Bennett, N. Perkins, L. Millard, J. Greaves, and A. Dickinson, *J. Catal.*, **2003**, 217, 427-433.
36. J. Yang, D. Wang, H. Han, and C. Li, *Acc. Chem. Res.*, **2013**, 46, 1900-1909.
37. D.Y. Leung, X. Fu, C. Wang, M. Ni, M.K. Leung, X. Wang, and X. Fu, *ChemSusChem*, **2010**, 3, 681-694.
38. L. Gomathi Devi and R. Kavitha, *Appl. Surf. Sci.*, **2016**, 360, 601-622.
39. D.B. Ingram and S. Linic, *J. Am. Chem. Soc.*, **2011**, 133, 5202-5205.
40. Z.W. Seh, S. Liu, M. Low, S.Y. Zhang, Z. Liu, A. Mlayah, and M.Y. Han, *Adv. Mater.*, **2012**, 24, 2310-2314.
41. C. Clavero, *Nat. Phot.*, **2014**, 8, 95-103.

42. G. Zhao, H. Kozauka, and T. Yoko, *Thin Solid Films*, **1996**, 277, 147-154.

43. Y. Tian and T. Tatsuma, *J. Am. Chem. Soc.*, **2005**, 127, 7632-7637.

44. Y. Ohko, T. Tatsuma, T. Fujii, K. Naoi, C. Niwa, Y. Kubota, and A. Fujishima, *Nat. Mater.*, **2003**, 2, 29-31.

45. A. Primo, A. Corma, and H. Garcia, *Phys. Chem. Chem. Phys.*, **2011**, 13, 886-910.

46. S. Zhang, J. Li, H. Niu, W. Xu, J. Xu, W. Hu, and X. Wang, *ChemPlusChem*, **2013**, 78, 192-199.

47. Y. Wang, J. Zhang, L. Liu, C. Zhu, X. Liu, and Q. Su, *Mat. Lett.*, **2012**, 75, 95-98.

48. L. Huang, F. Peng, H. Wang, H. Yu, and Z. Li, *Cat. Comm.*, **2009**, 10, 1839-1843.

49. D. Barreca, G. Carraro, A. Gasparotto, C. Maccato, M.E.A. Warwick, K. Kaunisto, C. Sada, S. Turner, Y. Gönüllü, T.-P. Ruoko, L. Borgese, E. Bontempi, G. Van Tendeloo, H. Lemmetyinen, and S. Mathur, *Adv. Mater. Interfaces*, **2015**, 2.

50. A. Sarkar, A.K. Singh, G.G. Khan, D. Sarkar, and K. Mandal, *RSC Adv.*, **2014**, 4, 55629-55634.

51. S. Banerjee, S.K. Mohapatra, P.P. Das, and M. Misra, *Chem. Mater.*, **2008**, 20, 6784-6791.

52. J. Yu, G. Dai, and B. Huang, *J. Phys. Chem. C*, **2009**, 113, 16394-16401.

53. K. Shankar, G.K. Mor, H.E. Prakasam, S. Yoriya, M. Paulose, O.K. Varghese, and C.A. Grimes, *Nanotechnology*, **2007**, 18.

54. A.D. Taylor, J. Ladd, Q. Yu, S. Chen, J. Homola, and S. Jiang,

Biosens. Bioelectron., **2006**, 22, 752-758.

55. J. Matsui, K. Akamatsu, N. Hara, D. Miyoshi, H. Nawafune, K. Tamaki, and N. Sugimoto, *Anal. Chem.*, **2005**, 77, 4282-4285.
56. S.C. Warren and E. Thimsen, *Energy Environ. Sci.*, **2012**, 5, 5133-5146.
57. K.R. Catchpole and A. Polman, *Appl. Phys. Lett.*, **2008**, 93.
58. L. Zhao, K.L. Kelly, and G.C. Schatz, *J. Phys. Chem. B*, **2003**, 107, 7343-7350.
59. K.-H. Su, Q.-H. Wei, J.J. Mock, D.R. Smith, X. Zhang, and S. Schultz, *Nano Lett.*, **2003**, 3, 1087-1090.
60. K. Wu, W.E. Rodriguez-Cordoba, Y. Yang, and T. Lian, *Nano Lett.*, **2013**, 13, 5255-5263.
61. H.A. Atwater and A. Polman, *Nat. Mater.*, **2010**, 9, 205-213.
62. J.H. Bang and P.V. Kamat, *ACS Nano*, **2009**, 3, 1467-1476.
63. C. Harris and P.V. Kamat, *ACS Nano*, **2009**, 3, 682-690.
64. J. Zhang, J.H. Bang, C. Tang, and P.V. Kamat, *ACS Nano*, **2010**, 4, 387-395.
65. G. Hodes, I.D.J. Howell, and L.M. Peter, *J. Electrochem. Soc.*, **1992**, 139, 3136-3140.
66. Q. Xiang, J. Yu, and M. Jaroniec, *J. Am. Chem. Soc.*, **2012**, 134, 6575-6578.
67. R.T. Tung, *Phys. Rev. Lett.*, **1984**, 52, 461-464.
68. J.D. Spengler and K. Sexton, *Science*, **1983**, 221, 9-17.
69. C.A. Redlich, J. Sparer, and M.R. Cullen, *The Lancet*, **1997**, 349, 1013-1016.
70. P. Wargocki, D.P. Wyon, Y.K. Baik, G. Clausen, and P.O. Fanger,

Indoor Air, **1999**, 9, 165-179.

71. F. Batault, F. Thevenet, V. Hequet, C. Rillard, L. Le Coq, and N. Locoge, *Chem. Eng. J.*, **2015**, 264, 197-210.

72. J. Torrero, F.J. Pérez-Alonso, M.A. Peña, C. Domínguez, A.O. Al-Youbi, S.A. Al-Thabaiti, S.N. Basahel, A.A. Alshehri, and S. Rojas, *ChemElectroChem*, **2016**, 3, 1072-1083.

국 문 초 록

이산화티탄 기반의 나노구조체들은 광촉매, 광전지(태양전지) 등의 태양광 에너지 전환과 친환경적 오염물 분해 등의 환경 문제 해결을 위한 우수한 물질로서 각광받아 왔다. 경제성, 우수한 물리화학적 안정성, 띠 간격 조절이 용이하다는 장점들은 이산화티탄이 다른 광전환 물질들에 비해 주목받게 하였다. 무한한 자원인 태양광을 이용하여 에너지와 환경 분야에 응용하는 것은 신재생 에너지를 활용하여 석유자원의 한계, 환경 오염의 문제를 넘어서는 해결책을 제시할 수 있기에 굉장히 중요한 기술이다. 따라서 이산화티탄의 장점을 활용하는 것이 중요하지만, 태양광 에너지의 상당 부분을 차지하는 가시광선을 효과적으로 활용하기에 띠 간격이 넓으며(3.0 ~ 3.2 eV), 광여기된 전하들의 재결합으로 인해 광효율이 낮다는 한계가 있다. 본 학위논문은 위 문제들을 해결하기 위해 서로 다른 측면에서 광여기 최적화에 접근한 내용들을 다룬다. 광효율을 향상시키기 위한 구조적 측면에서의 접근, 전자구조 및 계면을 제어하는

물질적 측면에서의 접근을 포함하는 연구 내용을 제시하였다.

이산화티탄의 내재적 특성을 제어하지 않는 간접적인 방법으로, 이산화티탄 나노튜브 배열에 은 나노입자가 이종접합된 구조를 제작하였다. 규칙적인 배열의 이산화티탄 나노튜브 구조는 광결정의 특성을 지녀 물질의 띠 간격에 의한 흡광이 아닌 구조적인 흡광을 나타낸다. 선행된 유한차분 시간 영역법(FDTD) 시뮬레이션 결과를 기반으로, 구조적 흡광 영역과 은 나노입자의 플라즈모닉 흡광 영역이 일치하도록 이산화티탄 나노튜브의 구조를 설계 및 최적화 하였다. 흡광 영역이 일치된 이산화티탄 나노튜브 배열은 일치되지 않은 경우에 비해 400 nm 이상의 가시광 조사 하에서 약 3배 향상된 광전류 크기를 나타내었다. 연구 결과는 넓은 띠 간격을 지닌 이산화티탄을 포함하는 금속 산화물류 기반의 플라즈모닉 광에너지 전환 시스템에서 합리적인 구조 설계가 광여기 최적화에 중요한 요소임을 제시한다.

이산화티탄의 전자구조 및 계면을 제어하여 직접적으로 광여기된 나노 촉매의 성능을 최적화하는 방법으로, 금속 이종원소가 공촉매로서 접합된

이산화티탄 나노입자를 제조하여 기상 아세트알데히드 분해 반응에 응용하였으며, 표면 특성 분석을 통해 성능 향상의 원인을 파악하고자 하였다. 가시광 하에서 효과적으로 작동하게 함과 동시에 경제성을 확보하기 위하여 합성 조건을 최적화 하였다. 최적화된 나노 촉매에서, 아세트알데히드의 분해에 필수적인 Pt 나노입자의 함량은 기존 상용 촉매 대비 10 % 임에도 성능을 유지하였다.

주요어: 광여기, 태양광 에너지 전환, 이산화티탄 나노구조체, 태양광 에너지 전환, 표면 플라즈몬 공명 효과, 금속 공촉매, 기상 아세트알데히드 분해 반응

학 번: 2013-22530

List of publications

International Peer-Reviewed Papaers

1. S.-Y. Bae*, **S. Y. Lee***, J.-W. Kim, H. N. Umh, J. Jeong, S. Bae, J. Yi, Y. Kim†, and Jinhee Choi†, "Hazardous potential of perovskite solar cells technology for potential implementation of "Safe-by-Design"", *Scientific Reports*, **2018**, DOI: 10.1038/s41598-018-37229-8.
   (* Su-Yong Bae and Su Young Lee contributed equally to this work.)

2. S. Yu, **S. Y. Lee**, H. N. Umh, and J. Yi, "Energy conversion of sub-band-gap light using naked carbon nanodots and rhodamine B", *Nano Energy*, **2016**, 26, 479-487.

3. H. N. Umh*, S. Yu*, Y. H. Kim, **S. Y. Lee**, and J. Yi, "Tuning the Structural Color of a 2D Photonic Crystal using a Bowl-Like Nanostructure", *ACS Applied Materials & Interfaces*, **2016**, 8(24), 15802-15808.

4. S. Yu, **S. Y. Lee**, J. Yeo, J. W. Han, and J. Yi, "Kinetic and Mechanistic Insights into the All-Solid-State Z-Schematic System", *The Journal of Physical Chemistry C*, **2014**, 118(51), 29583-29590.

5. S. Yu, Y. H. Kim, **S. Y. Lee**, H. D. Song, and J. Yi, "Hot-Electron-Transfer Enhancement for the Efficient Energy Conversion of Visible Light", *Angewandte Chemie-International Edition*, **2014**, 53(42), 11203-11207.

Patents

1. 이종협, 엄하늬, 유성주, 김용화, **이수영**, “구조색을 지닌 이산화티탄 나노기공성 필름 및 그 제조방법”, 대한민국특허 **등록** 10-1753529 (2017.07.04)
2. 이종협, 유성주, 김용화, **이수영**, 송현돈, “가시광선 범위의 광에너지 변환을 위한 3성분계로 이루어진 플라즈모닉 코어-쉘 나노구조체 및 그 제조방법”, 대한민국특허 **등록** 10-1724391 (2017.04.07)

International Conferences

1. **S. Y. Lee**, S. Yu, H. N. Umh, S. Shin, S. E. Jerng, and J. Yi, FRET-Assisted Upconversion of Organic Quantum Dots for the Utilization of Below-Bandgap Solar Energy, 2016 MRS Fall Meeting Program & Exhibit, Boston, Massachusetts, USA, Nov. 27-Dec. 2 (2016)
2. H. N. Umh, S. Yu, Y. H. Kim, **S. Y. Lee**, H. D. Song, and J. Yi, Realization of Inorganic Structrual Colors of a 2D Photonic Crystal, 2016 MRS Fall Meeting Program & Exhibit, Boston, Massachusetts, USA, Nov. 27-Dec. 2 (2016)
3. S. Yu, **S. Y. Lee**, Y. H. Kim, H. N. Umh, and J. Yi, Z-Schematic Electron-Transfer Kinetics of the All-Solid-State Photocatalyst Working at Visible Light, 27th International Conference on Photochemistry, ICC Jeju, Jeju Island, Korea, June. 28-July. 3 (2015)

4. S. Yu, **S. Y. Lee**, Y. H. Kim, H. N. Umh, J. Park, and J. Yi, Reaction Routes and Electron Transfer at Hetero-Interfaces of Catalysts for Artificial Photosynthesis, The 15th Korea-Japan Symposium on Catalysis, BEXCO and Haeundae Centum Hotel, Busan, Korea, May. 26-May. 28 (2015)

5. **S. Y. Lee**, S. Yu, J. W. Han, and J. Yi, Charge Transfer Kinetics of The Visible-Light Responsive Photocatalyst, The Korean Society of Clean Techonology 2014 Fall Meeting, K hotel, Gyeongju, Korea, Sep. 24-26 (2014)

6. S. Yu, Y. H. Kim, **S. Y. Lee**, H. N. Umh, and J. Yi, Photocatalytic Hydrogen Production via Water Splitting Using Nanomaterial Based Semiconductors, The Korean Society of Clean Techonology 2014 Fall Meeting, K hotel, Gyeongju, Korea, Sep. 24-26 (2014)

7. S. Yu, Y. H. Kim, **S. Y. Lee**, H. D. Song, H. N. Umh, and J. Yi, Plasmon-enhanced solar energy conversion to chemical and electrical energy, 248th American Chemical Society National Meeting & Exposition, San Francisco, CA, USA, Aug. 10-14 (2014)

8. I. Nam, G.-P. Kim, S. Park, J. W. Han, S. Bae, S. Yu, H. N. Umh, **S. Y. Lee**, Y. H. Kim, and J. Yi, High voltage energy storage systems using facile patterning approach, 248th American Chemical Society National Meeting & Exposition, San Francisco, CA, USA, Aug. 10-14 (2014)

9. J. Baek, T. Y. Kim, I. Nam, S. Park, S. Yu, S. Bae, **S. Y. Lee**, H. N. Umh, Y. H. Kim, and J. Yi, Production of valuable chemicals (1,3-butadiene) from biomass-based resources alternative to the petroleum, 248th American Chemical Society National Meeting & Exposition, San Francisco, CA, USA, Aug. 10-14 (2014)

10. S. Yu, Y. H. Kim, E. H. Kim, **S. Y. Lee**, and J. Yi, Facile preparation and characterization of graphene-modified carbon-doped TiO_2 nanopartides or a highly visible light responsive photocatalyst, 247th American Chemical Society National Meeting & Exposition, Dallas, Texas, USA, Mar. 16-20 (2014)
11. S. Yu, E. H. Kim, **S. Y. Lee**, Y. H. Kim, and J. Yi, Au Nanocatalyst Supported on the Fe-Doped TiO_2 Particles for High Activity in the CO Oxidation Reaction by a Mars-van Krevelen Mechanism, 2013 MRS Fall Meeting Program & Exhibit, Boston, Massachusetts, USA, Dec. 1-6 (2013)
12. E. H. Kim, S. Yu, J. Yeo, **S. Y. Lee**, Y. H. Kim and J. Yi, Analysis of cocatalyst on oxidative characteristics of visible-light responsive carbon-doped TiO_2 photocatalyst, The 14th Japan-Korea Symposium on Catalysis, WINC Aichi, Nagoya, Japan, July 1-3 (2013)

Domestic Conferences

1. 김용화, 정성은, 유영근, 박종석, 엄하늬, 배성준, **이수영**, 김영훈, 최진희, 이종협, Environmental Impact Analysis of Perovskite and Silicon Solar Cell via Life-cycle Assessment, 페로브스카이트 포토닉스 학술대회, 라마다프라자제주호텔, 11. 20-21 (2017)
2. **이수영**, 엄하늬, 배성준, 유영근, 박종석, 김용화, 정성은, 김영훈, 최진희, 이종협, Environmental Safety Assessment of Perovskite Solar

Cell, 페로브스카이트 포토닉스 학술대회, 2017년도, 라마다프라자 제주호텔, 11. 20-21 (2017)

3. 배성준, 유영근, 박종석, 송현돈, 엄하늬, **이수영**, 김용화, 정성은, 이종협, 한정우, 지르코니아 표면 특성으로 인한 리튬산소전지의 방전생성물 안정화 연구, 한국화학공학회 2017년도 봄 총회 및 학술대회, 제주 ICC, 4. 26-28 (2017)
4. **이수영**, 유성주, 엄하늬, 송현돈, 신수지, 이종협, 유무기 접합 시스템을 통한 밴드갭 이하의 광에너지 전환, 한국화학공학회 2016년도 봄 총회 및 학술대회, 부산 BEXCO, 4. 27-29 (2016), **우수 구두발표상 수상**
5. 엄하늬, 유성주, 김용화, **이수영**, 송현돈, 김혜선, 신수지, 이종협, 나비 날개를 모사한 이산화티탄 나노튜브 표면의 구조색 제어, 한국화학공학회 2016년도 봄 총회 및 학술대회, 부산 BEXCO, 4. 27-29 (2016)
6. 유성주, **이수영**, 김용화, 엄하늬, 이종협, 물로부터 청정연료 수소 생산을 위한 광촉매의 반응기작, 2015년 한국청정기술학회 춘계 학술발표회, 부여 롯데리조트, 3. 26-27 (2015)
7. 유성주, 김용화, **이수영**, 엄하늬, 이종협, 물로부터 수소와 전기 생산을 위한 청정기술 개발, 2015년 한국청정기술학회 춘계 학술발표회, 부여 롯데리조트, 3. 26-27 (2015)

8. 유성주, 김용화, **이수영**, 박수민, 유영근, 박종석, 이종협, 플라즈몬 유도 열전자를 이용한 효율적 태양광 에너지 전환, 한국화학공학회 2014년도 가을 총회 및 학술대회, 대전컨벤션센터, 10. 23-24 (2014)
9. **이수영**, 유성주, 엄하늬, 남인호, 배성준, 한정우, 이종협, 인공광합성 시스템하에서의 전하 이동 및 표면 반응 메커니즘, 한국화학공학회 2014년도 가을 총회 및 학술대회, 대전컨벤션센터, 10. 23-24 (2014)
10. 유성주, 김용화, **이수영**, 송현돈, 이종협, 가시광의 효율적 에너지 전환을 위한 플라즈모닉 코어-쉘 나노구조체, 2014년 한국청정기술학회 춘계 학술발표회, 여수경도리조트, 3. 27-28 (2014)
11. 유성주, 김용화, 김혜선, **이수영**, 이종협, 그래핀/탄소도핑 TiO_2 나노복합체 합성 및 이를 이용한 페놀분해, 한국화학공학회 2013년도 가을 총회 및 학술대회, 대구 EXCO, 10. 23-25 (2013)
12. 유성주, 이민재, 김혜선, **이수영**, 김용화, 이종협, 물 산화반응에 적합한 표면구조의 질소도핑 TiO_2 나노입자 개발, 2013년 한국청정기술학회 추계 학술발표회, 제주 한화리조트, 9. 25-27 (2013)
13. 유성주, 김혜선, 여정은, **이수영**, 김용화, 이종협, TiO_2 나노입자의 가전자대 위치에 따른 물 산화반응, 한국화학공학회 2013년 봄 총회 및 학술대회, 광주 김대중컨벤션센터, 4. 24-26 (2013)

14. 김혜선, 유성주, 여정은, **이수영**, 김용화, 이종협, C-TiO_2 가시광 광촉매의 조촉매에 따른 산화특성분석, 한국화학공학회 2013년 봄 총회 및 학술대회, 광주 김대중컨벤션센터, 4. 24-26 (2013)
15. 여정은, **이수영**, 유성주, 김혜선, 김용화, 이종협, 광촉매 내 전자 이동 경로의 모델링 및 형광분석을 통한 정량화, 2013년 한국청정기술학회 춘계 학술발표회, 여수 경도리조트, 3. 28-29 (2013)
16. 유성주, 김혜선, 여정은, **이수영**, 김용화, 이종협, 일산화탄소 산화반응의 담체로서 철 도핑 이산화티탄의 도핑 수준에 따른 영향, 2013 년 한국청정기술학회 춘계 학술발표회, 여수 경도리조트, 3. 28-29 (2013)